An a posteriori , efficient, high-spectral resolution hybrid finite-difference method for compressible flows

4 authors:

Javier Fernández-Fidalgo
Universidad Politécnica de Madrid
10 PUBLICATIONS **84** CITATIONS

Xesús Nogueira
University of A Coruña
75 PUBLICATIONS **1,307** CITATIONS

Luis Ramirez
University of A Coruña
42 PUBLICATIONS **495** CITATIONS

Ignasi Colominas
University of A Coruña
190 PUBLICATIONS **2,395** CITATIONS

An *a posteriori*, efficient, high-spectral resolution hybrid finite-difference method for compressible flows

Javier Fernández-Fidalgo[a,*], Xesús Nogueira[a,*], Luis Ramírez[a], Ignasi Colominas[a]

[a]*Universidade da Coruña,Group of Numerical Methods in Engineering, Campus de Elviña, 15071, A Coruña, Spain*

Abstract

A high-order hybrid method consisting of a high-accurate explicit finite-difference scheme and a Weighted Essentially Non-Oscillatory (WENO) scheme is proposed in this article. Following this premise, two variants are outlined: a hybrid made up of a Finite Difference scheme and a compact WENO scheme (CRWENO 5), and a hybrid made up of a Finite Difference scheme and a non-compact WENO scheme (WENO 5). The main difference with respect to similar schemes is its *a posteriori* nature, based on the Multidimensional Optimal Order Detection (MOOD) method. To deal with complex geometries, a multi-block approach using Moving Least Squares (MLS) procedure for communication between meshes is used. The hybrid schemes are validated with several 1D and 2D test cases to illustrate their accuracy and shock-capturing properties.

Keywords: high-order schemes, compressible flows, overset grids, Finite Differences.

1. Introduction

The solution of partial differential equations in presence of strong shocks has always been a difficult task. Several techniques have been explored in order to achieve high-order results, with the consequential increase of computational cost. In this article we explore a new hybrid technique based on the *a posteriori* detection paradigm that combines a Finite Difference (FD)

---

*Corresponding author, e-mail: {javier.fernandez1,xnogueira}@udc.es

scheme and a Weighted Essentially Non-Oscillatory (WENO) scheme. Obviously the methodology presented in this article is not only restricted to the schemes we present, but can also be applied to any combination of finite difference and WENO schemes regardless of their order of accuracy and/or compactness.

The key idea is to combine a fast and accurate scheme that cannot deal with shocks, with a scheme that can deal with them accurately at the expense of a higher computational cost. The scheme that can deal with shocks will only be used on those areas where the fast and accurate scheme is unable to obtain a quality solution. Thus, it is crucial the accurate and reliable detection of the problematic zones.

To that matter, several methods combining FD with WENO schemes have been proposed in the literature. For instance, Costa and Don presented in [1] a hybrid method composed by a sixth order FD scheme and a fifth order WENO scheme for the smooth and discontinuous parts of the solution, respectively. The type of criterion used to switch from one scheme to the other relies on a sensor that detects the discontinuities in advance (*a priori* detection).

The approach proposed by Pirozzoli [2] combines a fifth-order compact upwind algorithm for the smooth parts of the flow with a fifth-order WENO scheme to capture discontinuities. The detection criterion is *a priori* as well, employing a threshold value to distinguish the smooth from the non-smooth zones.

As explained in [3], the drawback of these approaches is that the shock locations are predicted, and related to the *a priori* guesses there can be a loss of efficiency due to over-detection of problematic zones. This happens around critical points, where the denominator of the derivatives approaches zero, and the method switches to the WENO scheme. To decrease the over-dissipation associated with such a degeneration, dimensional parameters, which require tuning for different problems, have been introduced in these *a priori* approaches.

In this work, an *a posteriori* detection criterion based on the Multidimensional Optimal Order Detection (MOOD) method is proposed. The reader is referred to [4, 5] for details on the MOOD paradigm.

Our approach differs from the original MOOD because of the underlying schemes we use for the calculations. In the original MOOD method [4], a single scheme ranging from arbitrary high-order to first order is used, so that the reconstruction order of the problematic cells is gradually downgraded up

2

to first order in case all the others attempts have failed. In our approach, we combine two methods of similar order, but with a significant difference in terms of computational cost. The fastest method is not able to deal with shocks, whereas the other method can handle shock waves at the price of increasing the overall computational cost. This conceptual difference is why we do not label the proposed methodology as MOOD, since it is an *a posteriori* approach but the order of the chosen schemes is not downgraded.

In this work we also present an approach based on Moving Least Squares (MLS) to apply the numerical scheme to block-structured meshes.

The structure of the paper is as follows. First, the governing equations and the different numerical methods used are presented. Then, the *a posteriori* detection paradigm is introduced. In section 6 we present the MLS-based technique for multi-block grid, and then we present some numerical examples to show the accuracy, efficiency and robustness of the proposed hybrid schemes. Finally, conclusions are drawn.

2. Governing equations

The goal of this article is to solve the two-dimensional Euler equations in general coordinates for an inviscid, compressible, newtonian fluid. Following the general curvilinear transformation $(x, y) \rightarrow (\xi, \eta)$ as in [6], these equations are written in the following strong conservation form:

$$\frac{\partial \hat{\mathbf{U}}}{\partial t} + \frac{\partial \hat{\mathbf{F}}}{\partial \xi} + \frac{\partial \hat{\mathbf{G}}}{\partial \eta} = \mathbf{0} \tag{1}$$

where $\hat{\mathbf{U}}$ denotes the transformed vector of conservative variables, being the original vector $\mathbf{U} = (\rho, \rho u, \rho v, \rho E)^T$ and $\hat{\mathbf{F}}$ and $\hat{\mathbf{G}}$ are the generalized inviscid flux-vectors. Using the same notation as in [7], these vectors can be expressed as

$$\hat{\mathbf{U}} = \frac{1}{J} \begin{pmatrix} \rho \\ \rho u \\ \rho v \\ \rho E \end{pmatrix} \quad \hat{\mathbf{F}} = \frac{1}{J} \begin{pmatrix} \rho \hat{U} \\ \rho u \hat{U} + \xi_x p \\ \rho v \hat{U} + \xi_y p \\ (\rho E + p) \hat{U} \end{pmatrix} \quad \hat{\mathbf{G}} = \frac{1}{J} \begin{pmatrix} \rho \hat{V} \\ \rho u \hat{V} + \eta_x p \\ \rho v \hat{V} + \eta_y p \\ (\rho E + p) \hat{V} \end{pmatrix} \tag{2}$$

where ρ is the density, u and v are the velocity components along the x and y axes, p is the pressure, and E is the total energy per unit mass expressed

as

$$E = \frac{p}{\rho\,(\gamma - 1)} + \frac{1}{2}\left(u^2 + v^2\right) \tag{3}$$

In (3), γ is the ratio of specific heat coefficients of the gas/fluid (for an ideal, monatomic gas, $\gamma = 7/5$). The quantities ξ_x, ξ_y, η_x and η_y are the spatial metrics of the transformation between the physical domain (x, y) and the computational space (ξ, η), where the subscript denotes partial derivation.

The inverse metrics $(x_\xi,\ y_\xi,\ x_\eta$ and $y_\eta)$ can be obtained by analytic differentiation or finite differences when the exact expression of the mapping between the physical space and the computational domain, that is,

$$\begin{cases} x = x\,(\xi, \eta) \\ y = y\,(\xi, \eta) \end{cases}$$

is not available.

The Jacobian of the transformation is denoted as

$$J = \left| \frac{\partial\,(x, y)}{\partial\,(\xi, \eta)} \right| = \frac{1}{x_\xi y_\eta - x_\eta y_\xi} \tag{4}$$

and the following expressions apply:

$$\begin{aligned} \xi_x &= Jy_\eta \\ \xi_y &= -Jx_\eta \\ \eta_x &= -Jy_\xi \\ \eta_y &= Jx_\xi \end{aligned} \tag{5}$$

The contravariant velocity components $\hat{U}$ and $\hat{V}$, are expressed as the dot product between the velocity vector $\mathbf{u} = (u, v)$ and the gradient of each family of lines, $\nabla\xi = (\xi_x, \xi_y)^T$ and $\nabla\eta = (\eta_x, \eta_y)^T$.

$$\begin{aligned} \hat{U} &= (\xi_x u + \xi_y v) \\ \hat{V} &= (\eta_x u + \eta_y v) \end{aligned} \tag{6}$$

In this work we have used the sixth-order Compact Finite Differences, as in [8], to obtain the inverse metrics. In [9] it is advised that the scheme used to calculate these metrics should be at least of the same order of accuracy as the schemes employed in the calculation. The option of calculating the

4

inverse metrics with the (CR)WENO scheme has been also ruled out because of the use of biased stencils near the boundaries, and the subsequent loss of accuracy.

3. Base Numerical Methods and Techniques

In this section we review the different schemes we use in our new hybrid formulation for the resolution of the Euler equations. This scheme is based on the use of an explicit, Low Dispersion Finite Difference (LDFD) method for the smooth regions of the flow, and a WENO scheme for the rest of the domain.

In this work we use two different Weighted Essentially Non-Oscillatory schemes. Namely, a compact scheme (CRWENO 5) [10] and a non-compact scheme (WENO 5) [11]. It is worth noting that any other WENO scheme can be used in our approach.

Dispersion and dissipation diagrams of all the schemes involved are shown in figure 1, where we also have included the curves for the first order forward and fourth orden central finite differences for reference. Please note, that the LDFD scheme, as well as the first and fourth order standard finite differences, has no inherent dissipation and thus, there is no curve to plot in the diagram.
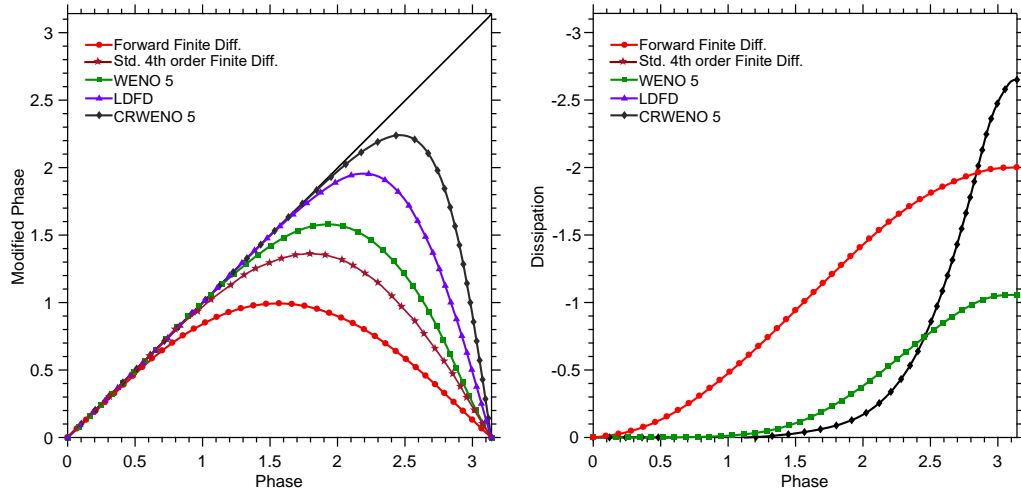

Figure 1: Dispersion (left) and dissipation (right) diagrams.

3.1. The base scheme: Low Dispersion Finite Difference (LDFD) scheme

In this work we have chosen the explicit, fourth order, centered, finite difference method defined and used by Bogey and Bailly in [12] as the base scheme. It has low dispersion error compared to the standard fourth order finite differences at the expense of a wider stencil.

When the LDFD scheme is used, the first derivative of the ξ-direction flux function $\hat{\mathbf{F}}$ at some interior node, is calculated as:

$$\left. \frac{\partial \hat{\mathbf{F}}}{\partial \xi} \right|_{i,j} \approx \sum_{p=0}^{N} s_p \left(\hat{\mathbf{F}}_{i+p,j} - \hat{\mathbf{F}}_{i-p,j} \right) \tag{7}$$

The value of the coefficients s_p is indicated in table 1. This scheme uses $N = 5$ nodes to each side of the central point, making an eleven-point stencil.

The derivative of the flux $\hat{\mathbf{G}}$ in the η-direction, is calculated using an analogous expression.

Table 1: Low Dissipation Finite Difference coefficients [12]

s_0	0.000000000
s_1	0.872756994
s_2	-0.286511174
s_3	0.090320001
s_4	-0.020779406
s_5	0.002484595

Due to the possible presence of shocks near or at the boundaries, in this work the preferred boundary scheme will be the Weighted Essentially Non-Oscillatory (either compact or non-compact) scheme at all times. Thus, no one-sided schemes are used here.

3.2. Filtering schemes

The base scheme in this work (LDFD), has not any inherent dissipation, as seen in figure 1. In order to use this scheme in convection dominant problems, a mechanism to introduce dissipation is required to stabilize the scheme. Here, compact filters proposed by Visbal and Gaitonde in [13] are used.

The filtered value of a function u, denoted as $\bar{u}$, is obtained by solving a tridiagonal system.

$$\alpha_{\mathrm{f}}\bar{u}_{i-1} + \bar{u}_i + \alpha_{\mathrm{f}}\bar{u}_{i+1} = \sum_{n=0}^{N} \frac{a_n}{2}\left(u_{i+n} + u_{i-n}\right) \tag{8}$$

In equation (8), α_{f} is kept as a free parameter and it regulates the amount of dissipation introduced by the filter, as shown in figure 2. The coefficients a_n depend on the order of the filter and can be found in [13] as well. As the LDFD scheme is not used here for boundary nodes, no special one-sided formulas are required.

The spectral function of the filter is obtained as [13]

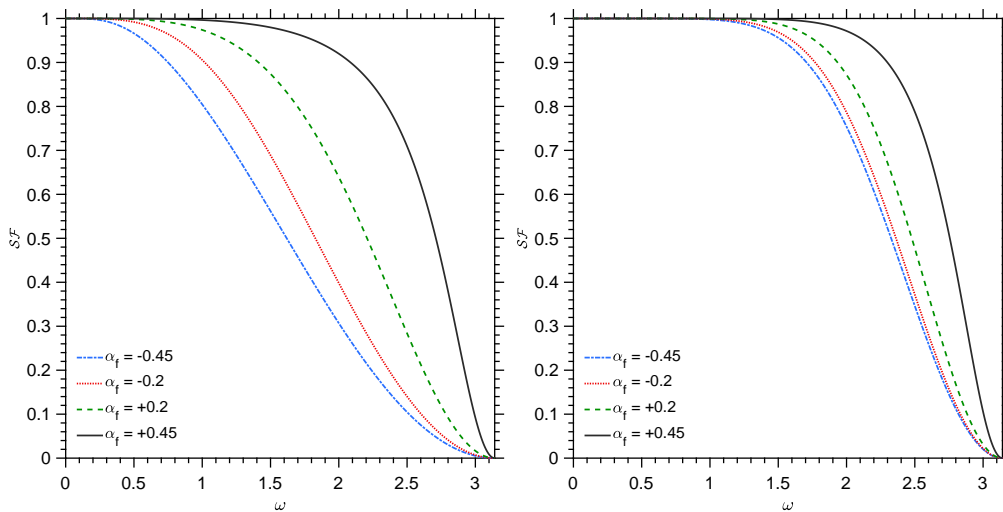$$\mathcal{SF}(\omega) = \frac{\displaystyle\sum_{n=0}^{N} a_n \cos(n\omega)}{1 + 2\alpha_{\mathrm{f}}\cos(\omega)} \tag{9}$$

Figure 2: Spectral functions of a fourth order filter (left) and a tenth order filter (right) for different values of α_{f}. The horizontal axis has been normalized between 0 and π.

Note that the filtering procedure is included to stabilize the numerical scheme for convection dominant problems. However, it is not enough to stabilize the LDFD numerical scheme in presence of shocks.

Different strategies to stabilize the scheme in presence of shocks have been proposed in the literature. Visbal and Gaitonde [13, 14], propose to use an adaptive filtering scheme, systematically reducing the order of the filter while increasing the value of the parameter α_f when approaching a shock region. Lo et al.[15] follow the same philosophy but they switch to Harten's first-order artificial compression method (ACM) [16] within the shock region. In this context, the use of high-order nonlinear filters for long time integration of DNS and LES of turbulent flows for both shock-free turbulence and turbulence-shock waves interactions has been presented in [17, 18]. A different approach consists in introducing numerical dissipation in the form of artificial diffusivity [19, 20], and solving the regularized system of equations with a high-order method. Hybrid *a priori* approaches [2, 21], consist in detecting the troubled zones around shocks and apply the shock-capturing schemes only on the detected regions. In order for the shock detectors to be valid and reliable, one has to be sure that at least all troubled zones are flagged as invalid. This approach usually sacrifices some efficiency in favour of the robustness of the algorithm In [22] the interested reader can find a thorough overview on these strategies.

In this work we propose a different approach, related to the aforementioned hybrid approaches. We use a WENO-family scheme to deal with non-smooth regions, as [21], but the region where the WENO scheme is used is determined *a posteriori* after the filtering step, only at regions where the solution is not acceptable. Two different WENO schemes are studied here, namely, the WENO 5 [10] and CRWENO 5 [11].

In this article, we usually use a tenth order filter for the computations with a value of $\alpha_f = 0.45$, except where explicitly indicated. A different choice of the filter and parameter indicates that more dissipation was required.

3.3. WENO 5

The formulation of the WENO 5 scheme used in this article, follows the original implementation by Jiang and Shu in [11], with the mapping proposed by Henrick et al. in [23]. The idea is to obtain a high-order interpolation of the fluxes at the interfaces midway between nodes (noted with half index values) and calculate the first derivative as

$$\left.\frac{\partial \hat{\mathbf{F}}}{\partial \xi}\right|_{i,j} \approx \frac{\hat{\mathbf{F}}_{i+1/2,j} - \hat{\mathbf{F}}_{i-1/2,j}}{\Delta \xi} = \frac{\left(\hat{\mathbf{F}}_i^+ + \hat{\mathbf{F}}_{i+1}^-\right) - \left(\hat{\mathbf{F}}_{i-1}^+ + \hat{\mathbf{F}}_i^-\right)}{\Delta \xi} \tag{10}$$

Because of the flux vector splitting (explained in Appendix A) a right-biased and a left-biased reconstruction at the interface $i + 1/2$ have to be computed (marked with a plus and minus sign, respectively). For brevity, only the reconstruction procedure for the left-biased reconstruction is explained in Appendix B. The right-biased reconstruction can be calculated using a symmetric arrangement of the stencils, as seen in figure 3.

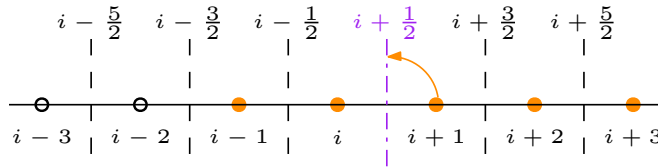Left-biased reconstruction
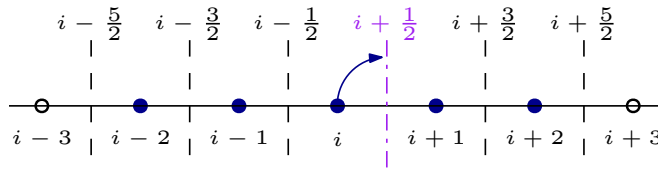
Right-biased reconstruction

Figure 3: WENO left-biased and right-biased reconstruction stencils.

The chosen implementation is in characteristic form as suggested by [11], because it is more robust and gives less oscillatory results in the presence of strong shocks.

3.4. CRWENO 5

The formulation of the CRWENO 5 scheme follows the implementation of Ghosh and Baeder in [10] with the same mappings proposed by Henrick et al. in [23]. This scheme follows the same idea as the WENO 5, but the candidate stencils have the interfaces implicitly related, which means a shorter stencil on the interior points.

An outline of the CRWENO 5 formulation can be consulted in Appendix C, and the complete formulation and adaptation to the Euler equations can be found in [10].

3.5. Temporal integration

The high-order spatial discretization step leads to a semi-discrete form that can be written as

$$\frac{\partial \left(\mathbf{U}/J \right)}{\partial t} = \mathbf{R} = - \left(\frac{\partial \hat{\mathbf{F}}}{\partial \xi} + \frac{\partial \hat{\mathbf{G}}}{\partial \eta} \right) \tag{11}$$

In this article we are not considering deforming or moving meshes so we can write

$$\frac{\partial \left(\mathbf{U}/J \right)}{\partial t} = \frac{\partial \mathbf{U}}{\partial t} \cdot \frac{1}{J} \tag{12}$$

and the final form of the ordinary differential equation can be written as

$$\frac{\partial \mathbf{U}}{\partial t} = \mathbf{R} = -J \left(\frac{\partial \hat{\mathbf{F}}}{\partial \xi} + \frac{\partial \hat{\mathbf{G}}}{\partial \eta} \right) \tag{13}$$

This ODE system can be solved in time with the total variation diminishing (TVD) three stage Runge Kutta (TVDRK3) as in [11], as follows:

$$\mathbf{U}^{(1)} = \mathbf{U}^n + \Delta t \mathbf{R}(\mathbf{U}^n)$$

$$\mathbf{U}^{(2)} = \frac{3}{4}\mathbf{U}^n + \frac{1}{4}\mathbf{U}^{(1)} + \frac{1}{4}\Delta t \mathbf{R}(\mathbf{U}^{(1)}) \tag{14}$$

$$\mathbf{U}^{n+1} = \frac{1}{3}\mathbf{U}^n + \frac{2}{3}\mathbf{U}^{(2)} + \frac{2}{3}\Delta t \mathbf{R}(\mathbf{U}^{(2)})$$

In generealized coordinates, the CFL is given by equation (15):

$$\mathrm{CFL} = \Delta t \left(\frac{\max\limits_{U} \left(|\xi_x u + \xi_y v| + c\sqrt{\xi_x^2 + \xi_y^2} \right)}{\Delta \xi} + \frac{\max\limits_{U} \left(|\eta_x u + \eta_y v| + c\sqrt{\eta_x^2 + \eta_y^2} \right)}{\Delta \eta} \right) \tag{15}$$

4. *A posteriori* HFDWENO and HFDCRWENO schemes

4.1. Overview

Since we aim to build a hybrid scheme, we need to develop a robust criterion capable of detecting the instabilities and shocks in order to switch from the LDFD scheme to the Weighted Essentially Non-Oscillatory scheme. In this work, we base the method on *a posteriori* limiting paradigm [4, 5, 24, 25].

Figure 4 shows schematically our approach. At the beginning of each Runge-Kutta step, a *candidate* solution $\mathbf{U}^*$ is computed using the LDFD scheme, based on the solution obtained on the previous Runge-Kutta step. The low-pass filtering procedure can be performed in each Runge-Kutta step, or only at the end of the third step, as explained in [7]. In this work, the latter strategy is adopted. Next, a number of detectors are run on the candidate solution to check if it has some desirable properties (that we will discuss afterwards). If all the detectors are fulfilled, it means the solution at that point is acceptable and it is assumed as the solution at the next Runge-Kutta step. Conversely, if any of the detectors flag the solution as invalid, that point along with some stencil around it (see figure 5), is recalculated with the WENO 5 or CRWENO 5 scheme.

An extensive description of the usually employed detectors can be consulted in [26], here we will only describe the ones we employ in our formulation, outlined in figure 4.
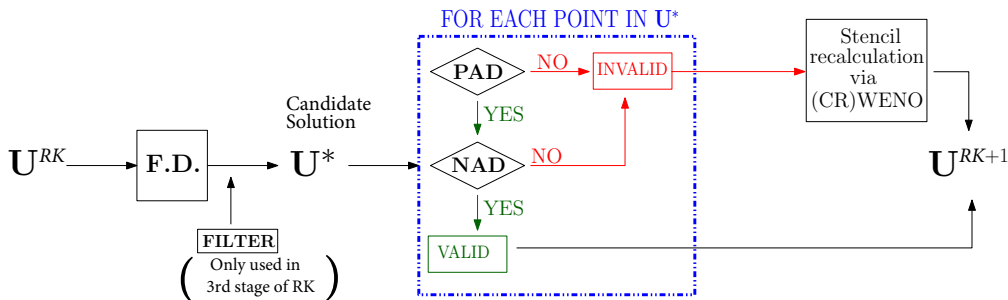

Figure 4: Present *a posteriori* approach. $\mathbf{U}^{\mathrm{RK}}$ represents a Runge-Kutta step and $\mathbf{U}^{\mathrm{RK+1}}$ represents the following step of the Runge-Kutta algorithm.

Physical Admissible Detector (PAD): This detector checks that the solution is physical, that is, all points must have positive density

11

and positive pressure at all times. In practice, this detector also identifies points with `NaN` values.

Numerical Admissible Detector (NAD) [24]: relaxed version of the Discrete Maximum Principle (DMP)[4]. It checks that the solution is monotonic and new extrema are not created. It compares the candidate solution with the solution obtained in the previous Runge-Kutta step. We remark that the superscript ^{n} indicates here the previous RK step, not the previous time step.

$$\min_{\mathbf{y}\in\mathcal{V}_i}\left(\mathbf{U}^n\left(\mathbf{y}\right)\right) - \delta \leqslant \mathbf{U}^*(\mathbf{x}) \leqslant \max_{\mathbf{y}\in\mathcal{V}_i}\left(\mathbf{U}^n\left(\mathbf{y}\right)\right) + \delta \tag{16}$$

$$\delta = \max\left(10^{-4}, 10^{-3}\cdot\left(\max_{\mathbf{y}\in\mathcal{V}_i}\left(\mathbf{U}^n\left(\mathbf{y}\right)\right) - \min_{\mathbf{y}\in\mathcal{V}_i}\left(\mathbf{U}^n\left(\mathbf{y}\right)\right)\right)\right) \tag{17}$$

The collection of points $\mathcal{V}_i$ represents the set of first neighbours of the point in consideration.

This implies that the candidate value remains between the local minimum and local maximum on the previous time step. In this work, the NAD is checked in the full conservative variables vector as suggested by [5].

The points that do not fulfill any of the employed detectors, are recalculated along with a stencil around them, as indicated in figure 5. The stencil size coincides with that of the fast Finite Differences scheme employed to calculate the candidate solution, and serves as an exclusion zone so that it is guaranteed that no LDFD stencil containing the flagged point is used across a shock.
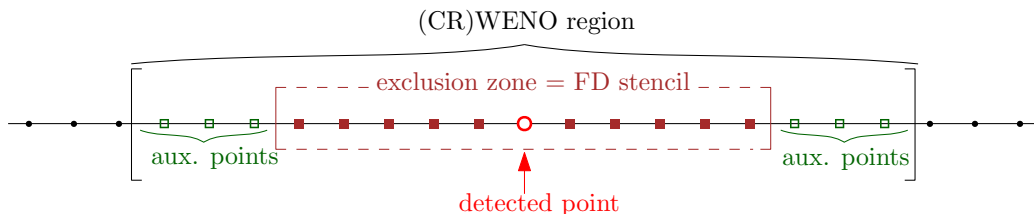

Figure 5: (CR)WENO recalculated region.

In figure 5 only the detected point and the nodes represented as solid brown squares are recalculated, but 3 more points on each end of the region (represented as green hollow squares) are needed in order to compute all the

interfaces required by the WENO or CRWENO schemes. The solution values in these auxiliary points are taken as the ones in the previous Runge-Kutta step.

If there is a number of detected nodes too close to each other that there is not enough space to create the region shown in figure 5, one can proceed as follows:

   1 Detect problematic points.

      ——————

  2.1 Form region around point 1.

  2.2 Form region around point 2.

     ...

  2.n Form region around point n.

      ——————

   3 Join all regions.

For a better understanding, the previous algorithm is illustrated in figure 6 for just two problematic points, but the generalisation is trivial.
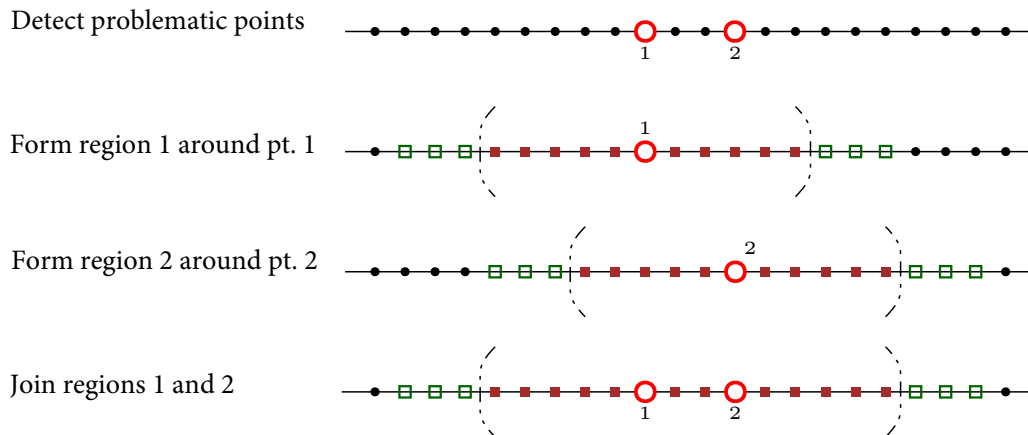
Figure 6: Region overlapping treatment for two points.

The boundary points that share an interface between (CR)WENO regions and LDFD regions have to be treated carefully in order not to generate spurious oscillations between the schemes. As seen in figure 7, the hollow circles denote the boundary points, and the thickest lines denote the boundary interfaces. In our formulation, the derivative of the flux at the nodes denoted as $A - 1$ and $B + 1$ is recalculated as

$$
\begin{aligned}
\left.\frac{\partial \hat{\mathbf{F}}}{\partial \xi}\right|_{A-1,j} &\approx \frac{\hat{\mathbf{F}}_{A-1/2,j} - \hat{\mathbf{F}}_{A-3/2,j}}{\Delta \xi} \\
\left.\frac{\partial \hat{\mathbf{F}}}{\partial \xi}\right|_{B+1,j} &\approx \frac{\hat{\mathbf{F}}_{B+3/2,j} - \hat{\mathbf{F}}_{B+1/2,j}}{\Delta \xi}
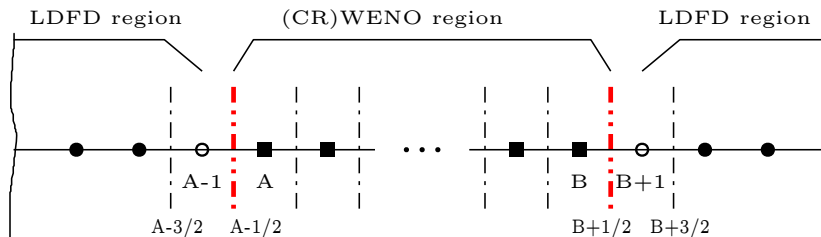\end{aligned}
\tag{18}
$$

Figure 7: Shared interface treatment between (CR)WENO and LDFD regions.

where $\hat{\mathbf{F}}_{A-1/2,j}$ and $\hat{\mathbf{F}}_{B+1/2,j}$ are the interface fluxes calculated via the (CR)WENO scheme, using (10). The computation of the interface fluxes $\hat{\mathbf{F}}_{A-3/2,j}$ and $\hat{\mathbf{F}}_{B+3/2,j}$, which are within the LDFD domain, can be done either by recasting the LDFD scheme in a finite volume style as presented in the appendix of [27], or by applying (7) to the discrete primitive of $\hat{\mathbf{F}}$ as explained in [28].

4.2. Positivity preserving flux limiters for WENO and CRWENO schemes

Given that the Weighted Essentially Non-Oscillatory schemes, that is, the WENO 5 or the CRWENO 5, are the last reconstruction procedures before entering the next Runge-Kutta step, we have to be able to guarantee the positivity of density and pressure after this step.

A possible choice to assure the positivity of density and pressure is to apply cut-off flux limiters [29] for density and pressure in an *a posteriori*

14

fashion. The basic idea proposed in [29] is to use the first order Lax-Friedrichs flux which has the positivity preserving property for CFL ≤ 0.5 and perform a weighted average between the (CR)WENO reconstructed flux and the Lax-Friedrichs flux so that the positivity of density and pressure is guaranteed. Here, we use a simpler approach, in which the (CR)WENO computed flux is completely replaced by the Lax-Friedrichs flux. This choice is less accurate than that proposed in [29], but it is faster in the computations. We note that in the test cases we have addressed, the (CR)WENO schemes failed in very few cells and in rather scarce time steps, so this choice is justified.

The positivity preserving algorithm is only applied if and only if the WENO or CRWENO schemes fail to produce a physical solution, and it is not involved in the process of generating the candidate solution.

In the numerical subsections, some quantitative information about the activation of the positivity preserving technique is given for each test case.

5. Boundary conditions

With regard to the hybrid scheme, seems reasonable to let the WENO 5 or CRWENO 5 schemes handle the boundary treatment because shocks can be present near the boundaries, and the LDFD scheme would not be able to properly handle these discontinuities. It is also possible to use one-sided formulas for the LDFD and the filtering schemes and then apply the (CR)WENO scheme in the boundary only if the base scheme fails, but this approach has not been addressed here.

The mesh is placed, as seen in figure 8, so that the physical boundaries of the domain coincide with the interface midway between mesh nodes. This arrangement is specially convenient when there is a wall boundary condition. Because of the WENO and CRWENO schemes, three layers of ghost nodes on each end of the mesh are needed. The ghost nodes are symmetrically placed taking the physical boundary as symmetry axis.
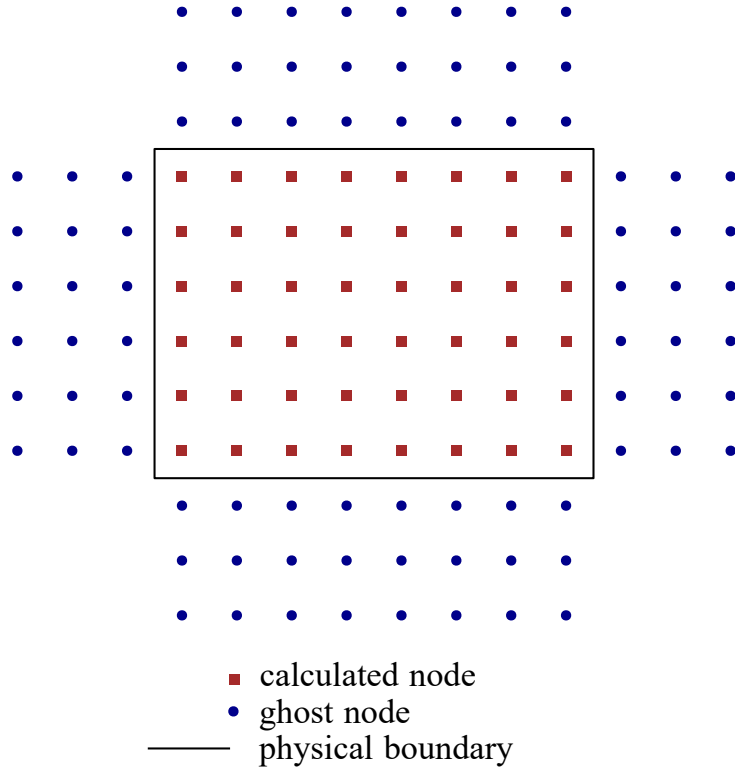
15

Figure 8: Schematic representation of the computational domain and node classification.

To explain some of the implemented boundary conditions, we will employ the notation shown in figure 9.
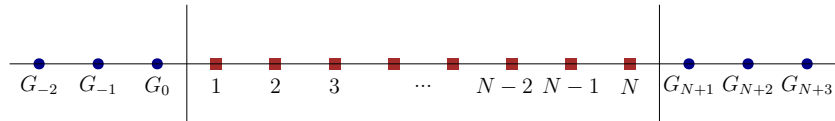

Figure 9: 1D sketch used for notation purposes for B.C.

Farfield boundary conditions: for the precise expressions used for these conditions, please refer to [30].

Inviscid wall boundary condition: given the special mesh placement, we use the so called "reflection technique", the values of ρ and ρE are mirrored using the interface where the values of the derivatives

16

should be zero as symmetry axis, as it can be seen in (20). This enforces the conditions:

$$\frac{\partial \rho}{\partial \mathbf{n}} = 0$$
$$\frac{\partial p}{\partial \mathbf{n}} = 0 \tag{19}$$

Regarding the velocity vector $\mathbf{u} = (u, v)^T$, the normal component with respect to the wall should be zero and the tangential derivative of the tangential component should be zero as well.

To wrap up, the expressions for the left end of the domain are

$$\rho^G_{1-j} = \rho_j$$
$$(\rho E)^G_{1-j} = (\rho E)_j \tag{20}$$

$$u^G_{1-j} = u_j - 2\left(\xi_x u_j + \xi_y v_j\right) \frac{\xi_x}{\xi_x^2 + \xi_y^2}$$
$$v^G_{1-j} = v_j - 2\left(\xi_x u_j + \xi_y v_j\right) \frac{\xi_y}{\xi_x^2 + \xi_y^2} \tag{21}$$

where $j = 1, 2, 3$ and the metrics have to be evaluated in the corresponding points, but the index has been omitted for clarity. The family of metrics involved in the calculations is the family normal to the wall.

Similar expressions for the right end of the domain can be obtained.

6. Multi-block meshes

For complicated geometries, sometimes it is more useful to employ several meshes to discretize the domain. This procedure allows us to place the meshes in a more convenient way for solving the numerical problem. With this technique, a very important problem arises: accuracy preservation in the procedure of communication between meshes.

17

Given that WENO and CRWENO schemes need three auxiliary nodes (ghost points) to perform the calculations, we take advantage of those nodes to communicate both meshes. To approximate the values at the ghost points, we employ the Moving Least Squares framework outlined in the following section, as done in [31, 32] for Finite Volume schemes.

6.1. Moving Least Squares (MLS)

This class of approximation methods reconstructs a given function from scattered, pointwise data [33]. In MLS, an arbitrary function $f(\mathbf{x})$ can be approximated as:

$$f(\mathbf{x}) \approx \hat{f}(\mathbf{x}) = \mathbf{p}^T(\mathbf{x})\,\mathbf{a}(\mathbf{x}) = \sum_{i=1}^{m} p_i(\mathbf{x})\,a_i(\mathbf{x}) \tag{22}$$

where $p_i(\mathbf{x})$ are basis functions, m is the total number of terms in basis functions, and $\mathbf{a}(\mathbf{x}) = [a_1(\mathbf{x}),\ldots,a_m(\mathbf{x})]^T$ is the coefficients vector.

Although the basis functions $\mathbf{p}(\mathbf{x}) = [p_1(\mathbf{x}),\ldots,p_m(\mathbf{x})]^T$ can be any kind of traditional function family, we chose them to be polynomials because of their simplicity. In two dimensions the linear, quadratic and cubic bases are represented in table 2.

Table 2: MLS 2D polynomial bases

	1	x	y	xy	x^2	y^2	x^2y	xy^2	x^3	y^3
Linear	●	●	●							
Quadratic	●	●	●	●	●	●				
Cubic	●	●	●	●	●	●	●	●	●	●

The main difference with respect to classic Least Squares (LS) approximation is that the coefficients $\mathbf{a}(\mathbf{x})$ vary with $\mathbf{x}$ in MLS and are constant throughout the domain in LS.

The deduction of the MLS coefficients can be seen in [33, 34] and will not be exposed here. The omitted calculations yield

$$\mathbf{a}(\mathbf{x}) = \underbrace{\left[\mathbf{P}^T\mathbf{W}\mathbf{P}\right]^{-1}}_{\mathbf{A}(\mathbf{x})} \cdot \underbrace{\left[\mathbf{P}^T\mathbf{W}\right]}_{\mathbf{B}(\mathbf{x})} \mathbf{f}(\mathbf{x}) = \mathbf{A}^{-1}(\mathbf{x})\,\mathbf{B}(\mathbf{x})\,\mathbf{f}(\mathbf{x}) \tag{23}$$

18

where:

$$\mathbf{f} = \begin{bmatrix} f\left(\mathbf{x}_1\right) \\ f\left(\mathbf{x}_2\right) \\ \vdots \\ f\left(\mathbf{x}_n\right) \end{bmatrix}$$

$$\mathbf{P} = \begin{bmatrix} \mathbf{p}^T\left(\mathbf{x}_1\right) \\ \mathbf{p}^T\left(\mathbf{x}_2\right) \\ \vdots \\ \mathbf{p}^T\left(\mathbf{x}_n\right) \end{bmatrix} = \begin{bmatrix} p_1\left(\mathbf{x}_1\right) & p_2\left(\mathbf{x}_1\right) & \cdots & p_m\left(\mathbf{x}_1\right) \\ p_1\left(\mathbf{x}_2\right) & p_2\left(\mathbf{x}_2\right) & \cdots & p_m\left(\mathbf{x}_2\right) \\ \vdots & \vdots & \ddots & \vdots \\ p_1\left(\mathbf{x}_N\right) & p_2\left(\mathbf{x}_N\right) & \cdots & p_m\left(\mathbf{x}_N\right) \end{bmatrix} \tag{24}$$

$$\mathbf{W} = \begin{bmatrix} W_1\left(\mathbf{x}-\mathbf{x}_1\right) & 0 & \cdots & 0 \\ 0 & W_2\left(\mathbf{x}-\mathbf{x}_2\right) & \cdots & 0 \\ \vdots & \vdots & \ddots & \vdots \\ 0 & 0 & \cdots & W_N\left(\mathbf{x}-\mathbf{x}_N\right) \end{bmatrix}$$
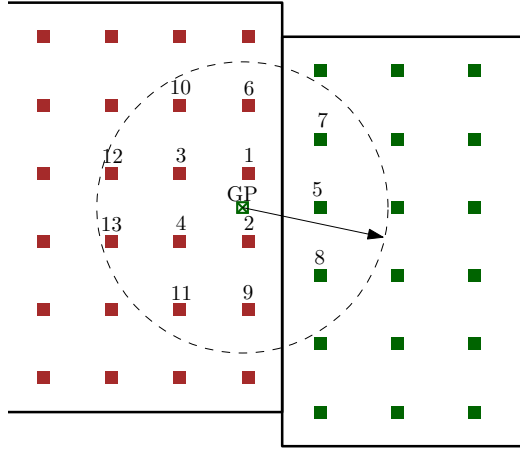

Figure 10: Compact support for the point GP using points from both meshes. The numbers above the nodes denote the order they are arranged in terms of distance to GP.

Finally, we can approximate the initial function as:

$$\hat{f}\left(\mathbf{x}\right) = \mathbf{p}^T\left(\mathbf{x}\right)\mathbf{a}\left(\mathbf{x}\right) = \underbrace{\mathbf{p}^T\left(\mathbf{x}\right)\mathbf{A}^{-1}\left(\mathbf{x}\right)\mathbf{B}\left(\mathbf{x}\right)}_{\boldsymbol{\Phi}(\mathbf{x})}\mathbf{f}\left(\mathbf{x}\right) = \boldsymbol{\Phi}\left(\mathbf{x}\right)\mathbf{f}\left(\mathbf{x}\right) \tag{25}$$

where $\boldsymbol{\Phi}(\mathbf{x})$ is commonly known as the MLS shape functions. We note that if the mesh position does not change with time, the shape functions do not vary as well.

Another important ingredient of MLS approximations is the kernel function W. There are many different kernel functions in the literature, but here we have used an exponential kernel function [25, 32, 35]. The role of the kernel function is to weight the importance of the different *neighboring* points in the approximation. The neighboring points are defined for each point $\mathbf{x}$ by the *support* of the kernel function. In this case, the support is a circle, as represented in figure 10 for a given point GP. For stability reasons, the minimum number of neighbors should be slightly higher than the number of elements of the polynomial basis. Here we have used a minimum number of 13 neighboring points for the cubic basis. The reader is referred to [32, 35] for more details.

6.2. Data communication procedure

The employed positioning of two meshes can be seen in figure 11. This arrangement only requires the interpolation of the ghost points to communicate both meshes. Given that they share a common edge, all real points from both meshes can be calculated as usual, and share the information between meshes using solely the ghost points. The reconstruction process uses points from both meshes, as shown in figure 11.
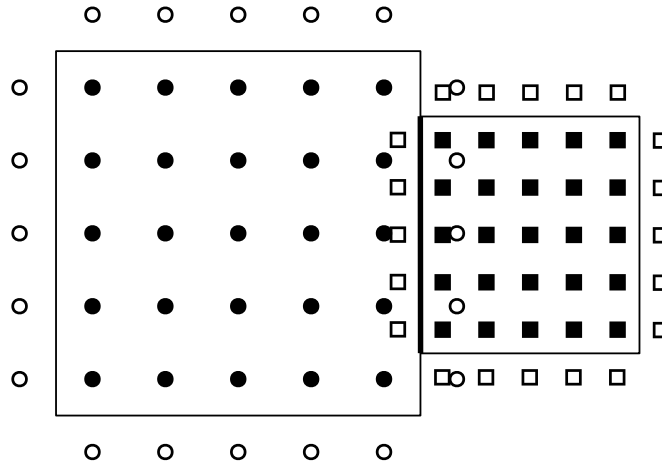

Figure 11: Mesh positioning schematic. For simplicity we only represent 1 ghost point on each direction, represented as hollow shapes.

20

MLS approximation is performed at a ghost point, using a neighborhood of points as explained in the previous section (see figure 10). The algorithm for each ghost point is outlined in table 3. The way the neighbouring points are selected is locating the nearest point to the ghost point (GP) in both meshes. Once the two points are located, given the structured nature of the grids, it is easy to locate a certain amount of neighbours of those points within their corresponding mesh. Finally we can sort the points from both meshes with respect to their distance to GP using any of the widely known sorting algorithms, resulting in the numeration we can see in figure 10.

Table 3: MLS Approximation Algorithm

(1)	Initial data: $\{\mathbf{x}_i, f(\mathbf{x}_i)\}$
(2)	Form basis functions $\mathbf{p}(\mathbf{x}) = [p_1(\mathbf{x}), \ldots, p_m(\mathbf{x})]^T$ and determine matrix $\mathbf{P}$
(3)	For each point: form the shape function

a)	Select weighting function
b)	Form matrix $\mathbf{W}$
c)	Obtain matrices $\mathbf{A}(\mathbf{x})$ and $\mathbf{B}(\mathbf{x})$
d)	Calculate $\mathbf{A}^{-1}(\mathbf{x})$
e)	Form shape function $\mathbf{\Phi}(\mathbf{x})$

End For each point

(4)	Approximate function using equation (26)

After the computation of the shape functions, the value of any of the conservative variables at the ghost point, are calculated as:

$$\mathbf{U}_{\mathrm{GP}} \approx \sum_{j=1}^{N} \Phi_j^{\mathrm{GP}} \mathbf{U}_j \tag{26}$$

where N stands for the total number of points used to perform the approximation.

This process has to be done whenever a relative displacement of the meshes takes place. Meaning that for static meshes, the interpolation nodes can be stored beforehand and save considerable computational effort.

In order to deal with the possible oscillations that can be generated throughout the process of approximation, and that can lead to the apparition of non-physical values in the solution, an analogous detection to that of the

PAD is performed within the MLS framework. Starting with a high-order d_0 polynomial basis, the MLS reconstruction is attempted. If the values of the density and pressure are physical, the reconstruction is accepted as valid. If the values are not physical, a lower order reconstruction is attempted. Obviously, the reconstruction of order 1 cannot produce any non-physical values given that all the values used in the interpolation are physical. A schematic explanation of the process can be seen in figure 12.
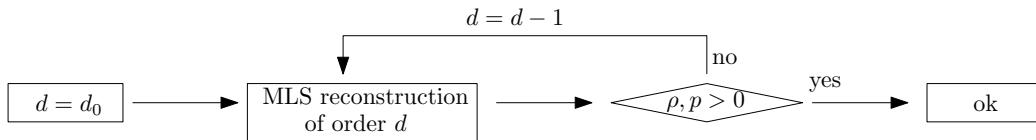

Figure 12: MLS reconstruction to avoid non-physical values, starting with a d_0 order basis.

7. Numerical examples

In this section several numerical examples computed with these new hybrid schemes are presented. In the first cases, the WENO 5 and CRWENO 5 (denoted simply as WENO and CRWENO from now on) are compared with the new hybrid schemes that are denoted as HFDWENO and HFDCRWENO, respectively.

For all test cases the value for the ratio of specific heat coefficients of the ideal gas is $\gamma = 7/5$, will be run at a constant CFL = 0.5, using a tenth order filter for the LDFD with $\alpha_f = 0.45$, and Global Lax-Friedrichs flux splitting unless otherwise noted.

7.1. Two-dimensional Entropy Wave Advection

This problem reproduces that contained in [36]. It simulates the advection of a density wave at a constant freestream velocity while the pressure and velocity remain unchanged. The analytical solution for this problem at a given time t is given by:

$$
\begin{aligned}
\rho(x, y, t) &= \rho_\infty + A \sin\left[\pi\left(x + y - (u_\infty + v_\infty)t\right)\right] \\
u(x, y, t) &= u_\infty \\
v(x, y, t) &= v_\infty \\
p(x, y, t) &= p_\infty
\end{aligned}
\tag{27}
$$

22

As the analytical solution is known, this example can be used to evaluate the order of accuracy of the schemes.

To evaluate the order of accuracy we use the following values for the parameters in equation (27):

$$A = 0.2 \qquad \rho_\infty = 1 \qquad u_\infty = 1 \qquad v_\infty = 0 \qquad p_\infty = 1 \qquad (28)$$

Next, we test each of the non-hybrid schemes separately and compute the L_2 norm for the density variable.

We tested two different mesh configurations covering the same domain, which is a 2 by 2 square, as seen in figure 13. For case A a single mesh where periodic boundary conditions will be used, whereas case B is run with two meshes communicated by the MLS procedure previously explained. For the latter case, periodic boundary conditions are used everywhere except on the shared side at $x = 1$, where the MLS procedure is used. A quintic polynomial basis is employed. In both cases $h_x = h_y = h$ and we use an even number of nodes, so that both configurations have the nodes in the exact same locations. For case B each of the two grids has the same number of nodes in the vertical direction as the single grid of case A. In order to keep the same spatial resolution in both configurations, the number of nodes in the horizontal direction of each mesh will be half of that in the vertical direction. The simulation is run until $t = 2.0$.

We use the global Lax-Friedrichs flux splitting explained in Appendix A. All the simulations are run with a CFL equal to 0.1. Please note that no detection criterion is activated and the positivity preserving technique does not activate for any of the cases in this example.
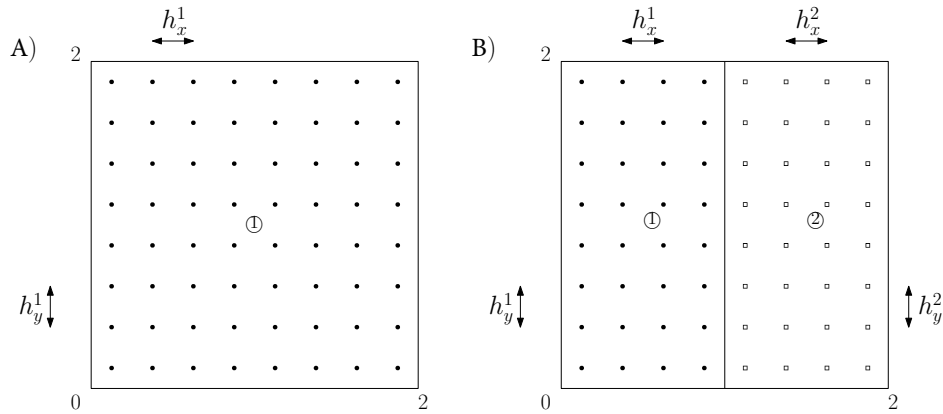
Figure 13: Two different mesh configurations for testing the order of accuracy in the 2D Entropy Wave test case. Case A: Single mesh. Case B: Two side-by-side meshes.

In tables 4, 5 and 6 we show the L_2 norm of the density error obtained for cases A and B. As expected, we recover the formal order of accuracy for the LDFD and WENO schemes, for case A. It is shown that the formal order of accuracy is not altered significantly employing the Moving Least Squares approximation for communication between meshes, that is, case B.

We also note that the LDFD scheme is remarkably faster than any of the WENO schemes, as expected.

Table 4: Entropy wave advection. LDFD results.

Points	Case A			Case B		
	L_2	r_2	Time (s)	L_2	r_2	Time (s)
20x20	1.5220E-05	—	0.50	1.5219E-05	—	1.08
40x40	1.1683E-06	3.70	3.05	1.1753E-06	3.69	6.47
60x60	2.3942E-07	3.91	9.33	2.3897E-07	3.93	18.54
80x80	7.6729E-08	3.96	21.48	7.7853E-08	3.90	40.42
100x100	3.1614E-08	3.97	39.43	3.2615E-08	3.90	75.48
200x200	1.9916E-09	3.99	342.03	2.1126E-09	3.95	563.34

Table 5: Entropy wave advection. WENO results.

Points	Case A			Case B		
	L_2	r_2	Time (s)	L_2	r_2	Time (s)
20x20	1.6663E-04	—	2.53	1.6653E-04	—	3.11
40x40	5.1463E-06	5.02	18.78	5.1400E-06	5.02	21.34
60x60	6.7928E-07	4.99	61.69	6.8215E-07	4.98	69.44
80x80	1.6150E-07	4.99	145.77	1.6066E-07	5.03	165.25
100x100	5.3013E-08	4.99	290.08	5.4367E-08	4.86	324.09
200x200	1.6756E-09	4.98	2442.30	1.7548E-09	4.95	2492.45

Table 6: Entropy wave advection. CRWENO results.

Points	Case A			Case B		
	L_2	r_2	Time (s)	L_2	r_2	Time (s)
20x20	2.6806E-05	—	8.89	2.9636E-05	—	9.40
40x40	7.4346E-07	5.17	65.14	7.9065E-07	5.23	70.32
60x60	9.6928E-08	5.02	211.67	1.0471E-07	4.99	217.20
80x80	2.3098E-08	4.99	589.06	2.3753E-08	5.16	610.13
100x100	7.6382E-09	4.96	1093.59	8.1425E-09	4.80	1128.21
200x200	2.5680E-10	4.89	7853.94	2.7837E-10	4.87	7895.38

This example illustrates that all the schemes used in this article recover their optimal order of accuracy for smooth problems. Moreover, the proposed methodology for multi-block meshes keeps the order of accuracy and the magnitude of the errors.

For better understanding of the execution times for the different schemes, in table 7 we show the extrapolated computational time for a given L_2 error of 1E-10.

Table 7: Extrapolated execution times for a given L_2 error of 1E-10

Time (s)	LDFD	WENO	CRWENO
Case A	2629	12207	14105
Case B	5248	12899	14271

7.2. Two Interacting Blast Waves

This one-dimensional problem involves multiple interactions of strong shocks and rarefactions with each other and with contact discontinuities. It is specially difficult to solve in a uniform Eulerian grid without the use of local refinement. The reader is referred to [37] for an in-depth analysis. In this test case we will test the proposed hybrid scheme and we compare its results with those obtained with the WENO schemes.

This problem takes place in a [0,1] domain with reflective boundary conditions at both ends, and with the following values for the primitive variables at $t = 0$:

$$(\rho, u, p) = \begin{cases} (\rho_L, u_L, p_L) & \text{if} & x \leq 0.1 \\ (\rho_M, u_M, p_M) & \text{if} & 0.1 < x < 0.9 \\ (\rho_R, u_R, p_R) & \text{if} & x \geq 0.9 \end{cases} \tag{29}$$

where:

$$\begin{aligned} (\rho_L, u_L, p_L) &= (1.0, 0.0, 1000.0) \\ (\rho_M, u_M, p_M) &= (1.0, 0.0, 0.01) \\ (\rho_R, u_R, p_R) &= (1.0, 0.0, 100.0) \end{aligned} \tag{30}$$

All the computations have been carried out with a CFL number of 0.5 for seven different grids ranging from 50 to 3200 nodes until $t = 0.038$.

The computations have been carried out with a tenth order filter with $\alpha_f = 0.45$

In table 8, we summarize the total computational time for both the non-hybrid and hybrid schemes, as well as a relative time percentage showing the actual time saving.

On the coarsest grids, the hybrid schemes can be slower than the original schemes. The poor space resolution of the mesh causes the detectors PAD and NAD to flag all the points in the domain for every iteration. The cost of updating the solution with a WENO or CRWENO scheme over the full domain is incremented by the cost of previously computing the candidate solution with the LDFD scheme.

Although this may be the case for coarse meshes, when the mesh is gradually refined the obtained computational time for the hybrid schemes is significantly lower than that of the original schemes.

Table 8: Two Interacting Blast Waves. Time comparative

CFL=0.5	Total Time (s)		Saved Time (%)	Total Time (s)		Saved Time (%)
Nodes	WENO	HFDWENO		CRWENO	HFDCRWENO	
50	0.03	0.02	—	0.06	0.05	—
100	0.08	0.07	4.87	0.27	0.19	29.41
200	0.31	0.23	25.00	1.11	0.58	47.89
400	1.25	0.83	33.75	4.42	1.78	59.72
800	5.08	2.70	46.77	17.39	5.72	67.12
1600	20.58	9.80	52.39	69.73	19.89	71.48
3200	81.47	37.47	54.01	287.14	71.48	75.10

This difficult test case was designed to illustrate the strong relationship between the accuracy of the overall flow solution and the sharp resolution of discontinuities. To this matter, it is shown that the two hybrid schemes behave very similarly to their corresponding original schemes, with a very significant difference in terms of computational cost. It is notable the time saving using both hybrid schemes, being the HFDCRWENO the one with higher rates of saving due to the fact that the CRWENO method requires more CPU time than the WENO scheme.

In figures 14 and 15, we present the results for the intermediate mesh of 400 nodes. In both cases the solution obtained employing the hybrid scheme, is very similar to the solution computed via the WENO and CR-WENO schemes, as it can be seen on the zoomed detail on the right of the figures. In those figures, the reference solution corresponds to the computation of the WENO scheme for a 21870 node grid. The detected nodes, at the bottom of the figure, refer to the nodes where the PAD or NAD have been activated on the last time step.
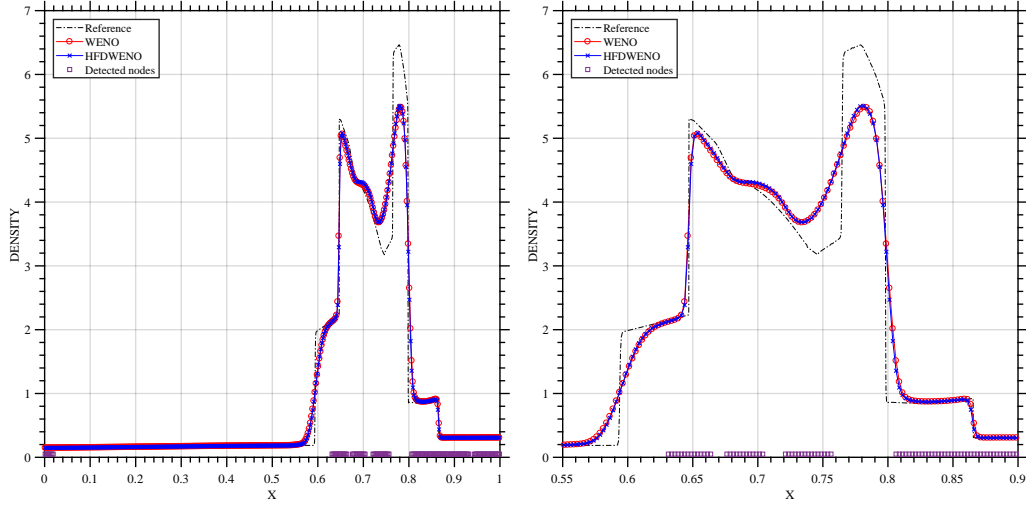
Figure 14: Two interacting Blast Waves. 400 nodes. Comparative between the density results obtained using the WENO scheme and the results obtained using the HFDWENO scheme (left) and zoomed in density results (right).
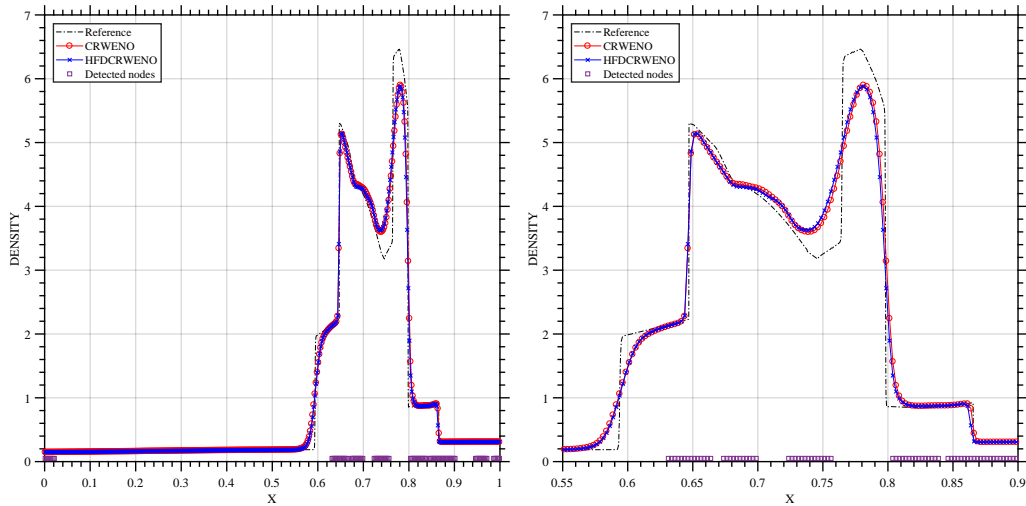

Figure 15: Two interacting Blast Waves. 400 nodes. Comparative between the density results obtained using the CRWENO scheme and the results obtained using the HFDCR-WENO scheme (left) and zoomed in density results (right).

In figure 16 we present an efficiency plot in the same manner of [38]. The error for the sequence of seven meshes is plotted versus the CPU time required

28

for the computations. It is observed than the magnitude of errors of the hybrid schemes is similar to that of the (CR)WENO methods. It is also seen that the hybrid schemes require less CPU time to obtain a given error. From the figure we observe that for the coarsest grids, the most efficient scheme is the HFDWENO. However, as the grid is refined, the HFDCRWENO is the most efficient scheme.
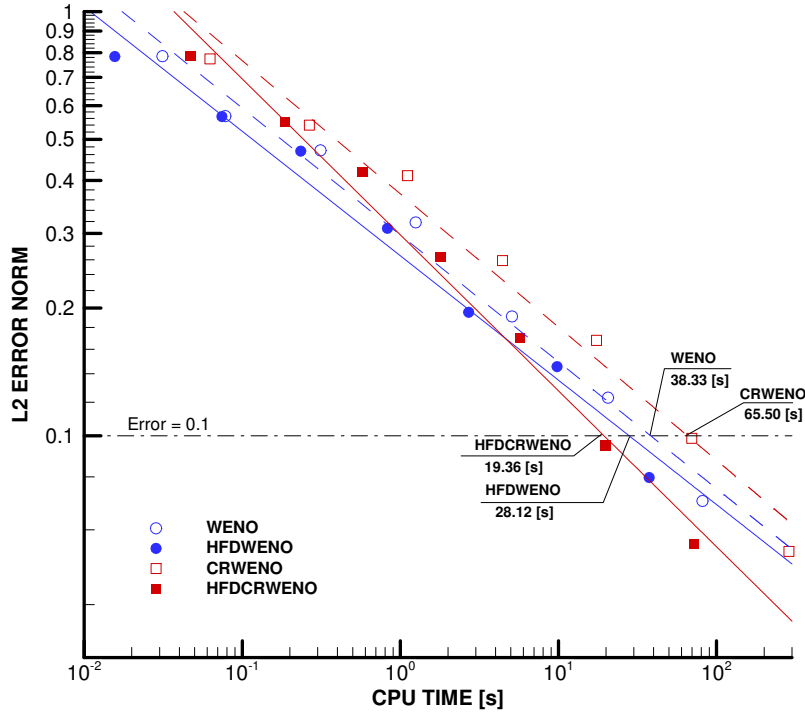
Figure 16: Two interacting Blast Waves. Efficiency plot: Error versus CPU time for a sequence of seven meshes. We also plot the CPU times corresponding to an error=0.1. It is seen that the hybrid schemes are more efficient than the (CR)WENO schemes.

For this case, the positivity preserving technique does not activate for the WENO and HFDWENO schemes, and it is only activated in a few nodes for the CRWENO and HFDCRWENO schemes when the two shocks interact.

7.3. Shock/Density Oscillation Interaction

This one-dimensional test case, proposed in [39], is a Mach 3 shock wave interacting with upstream sinusoidal density waves. The domain is defined

in $-5 \leq x \leq 5$ and the boundary conditions are set as inflow at $x = -5$ and outflow at $x = 5$.

The solution is computed with a CFL number equal to 0.5 and the final time of the simulation is $t = 1.8$. The computations have been carried out with a tenth order filter with $\alpha_f = -0.45$. We have chosen to use this parameter in order to increase the dissipation of the hybrid scheme. We have seen that this choice obtains the best results for this test case. For this case, the positivity preserving technique does not activate for any of the studied schemes.

The non-dimensional initial condition is defined as:

$$(\rho, u, p) = \begin{cases} (3.857143, 2.269369, 10.33333) & \text{if} \quad x < -4 \\ (1 + 0.2\sin(5x), 0, 1) & \text{if} \quad x \geq -4 \end{cases} \tag{31}$$

This test measures the ability of the schemes for capturing both small-scale smooth flow and shocks. CPU times are shown in Table 9. It shows that for coarse grids the hybrid schemes are slower than the original ones, but the time savings are really remarkable when the mesh is refined.

Table 9: Shock/Density Oscillation Interaction. Time comparative

CFL=0.5	Total Time (s)		Saved Time (%)	Total Time (s)		Saved Time (%)
Nodes	WENO	HFDWENO		CRWENO	HFDCRWENO	
50	0.02	0.02	—	0.05	0.05	—
100	0.05	0.05	—	0.14	0.09	33.33
200	0.19	0.13	33.33	0.59	0.25	57.89
400	0.70	0.36	48.89	2.38	0.70	70.39
800	2.83	1.23	56.35	9.41	2.03	78.41
1600	11.22	4.17	62.81	37.23	5.77	84.52
3200	44.50	15.28	65.66	154.67	18.73	87.89

In figures 17 and 18, it is seen that both hybrid and classical scheme solutions behave similarly. The reference solution corresponds to the computation of the WENO scheme for a 12800 node grid. The detected nodes refer to the nodes that did not pass the detection tests run on the LDFD candidate solution. No significant differences are observed between the hybrid schemes and their classic counterparts.
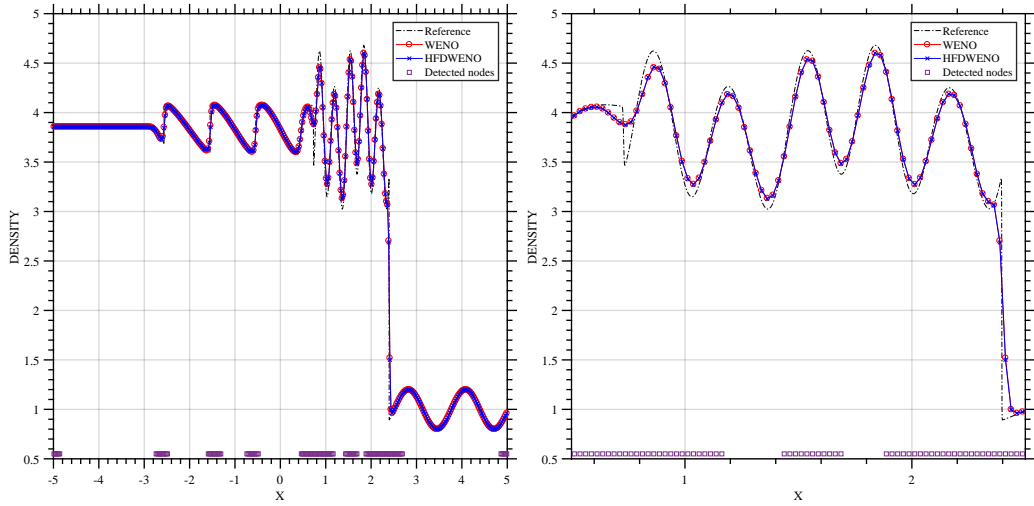
Figure 17: Shock/density Oscillation Interaction. 400 nodes. Comparative between the density results obtained using the WENO scheme and the results obtained using the HFDWENO scheme (left) and zoomed in density results (right).
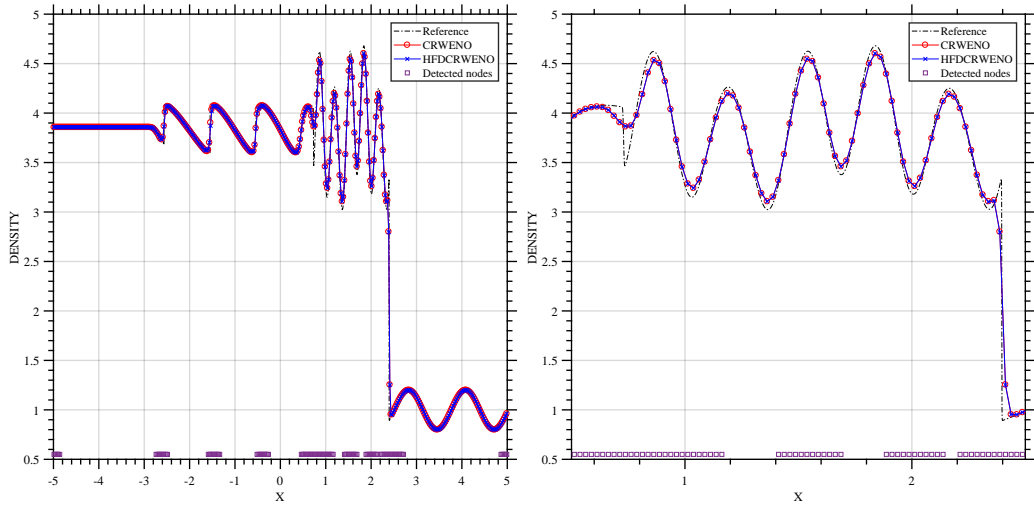

Figure 18: Shock/density Oscillation Interaction. 400 nodes. Comparative between the density results obtained using the CRWENO scheme and the results obtained using the HFDCRWENO scheme (left) and zoomed in density results (right).

In figure 19 we present the efficiency plot for this test case. The error for

31

the sequence of meshes is plotted versus the CPU time required for the computations. It is observed than the magnitude of errors of the hybrid schemes is similar to that of the (CR)WENO methods. It is also seen that hybrid schemes require less CPU time to obtain a given error. As in the previous test case, we observe that for the coarser grids the most efficient scheme is the HFDWENO, and the HFDCRWENO becomes the most efficient scheme as the grid is refined.
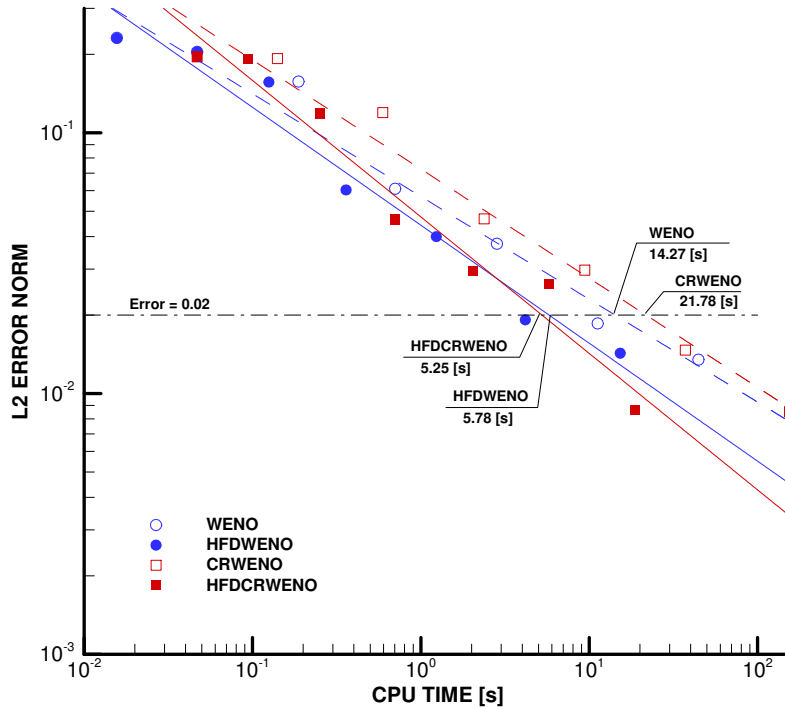
Figure 19: Shock/density Oscillation Interaction. Efficiency plot: Error versus CPU time for a sequence of seven meshes. We also plot the CPU times corresponding to an error=0.02. It is seen that the hybrid schemes are more efficient than the (CR)WENO schemes.

7.4. 2D Riemann Problem.

This family of cases takes place in a unitary square divided in four quadrants, each sector having different values for the primitive variables. Among all the possible configurations proposed in [40], we chose case F (re-labelled as case 12 in [41]).

In figure 20 the initial configuration is presented. The unit square is divided into 4 quadrants with different values of the primitive variables generating shocks and contact discontinuities across the borders. The simulation is run until $t = 0.25$, as referenced in [41].
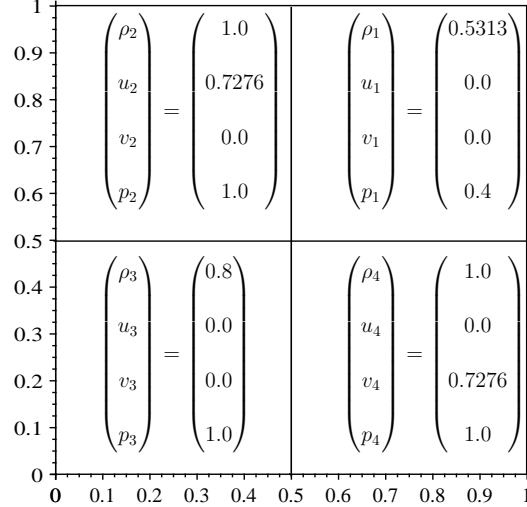

$$\begin{pmatrix} \rho_2 \\ u_2 \\ v_2 \\ p_2 \end{pmatrix} = \begin{pmatrix} 1.0 \\ 0.7276 \\ 0.0 \\ 1.0 \end{pmatrix} \qquad \begin{pmatrix} \rho_1 \\ u_1 \\ v_1 \\ p_1 \end{pmatrix} = \begin{pmatrix} 0.5313 \\ 0.0 \\ 0.0 \\ 0.4 \end{pmatrix}$$

$$\begin{pmatrix} \rho_3 \\ u_3 \\ v_3 \\ p_3 \end{pmatrix} = \begin{pmatrix} 0.8 \\ 0.0 \\ 0.0 \\ 1.0 \end{pmatrix} \qquad \begin{pmatrix} \rho_4 \\ u_4 \\ v_4 \\ p_4 \end{pmatrix} = \begin{pmatrix} 1.0 \\ 0.0 \\ 0.7276 \\ 1.0 \end{pmatrix}$$

Figure 20: 2D Riemann Problem. Initial setup.

The positivity preserving technique does not get activated for any of the studied schemes in the present test case.

The solutions to this configuration are symmetrical with respect to the $y = x$ diagonal, so this property is expected to be conserved by the numerical schemes.

As in the previously described cases, in table 10 we show a time comparative between the traditional and hybrid schemes. We draw the reader's attention to the great reduction in computational time obtained using the hybrid schemes.

Table 10: 2D Riemann Problem. Time comparative

CFL=0.5	Total Time (s)		Saved Time (%)	Total Time (s)		Saved Time (%)
Mesh	WENO	HFDWENO		CRWENO	HFDCRWENO	
100x100	17.94	11.39	36.51	57.99	31.32	46.00
200x200	155.15	73.19	52.82	508.56	168.12	66.94
400x400	1386.74	591.77	57.32	4254.87	926.71	78.22
800x800	11645.15	4665.63	59.93	34999.33	6033.53	82.76

The results for the density field in the finest grid are shown in figure 21, using a tenth order filter with $\alpha_f = 0.45$. It is observed that using the hybrid schemes vortical structures appear along the contact discontinuities. According to [42], this solution may not be physical. This kind of structures appear for very low dissipation schemes. Given the absence of analytic solution to this problem, and following the conclusions of [42], this indicates that the proposed schemes are a good choice for problems with complicated structures of multi-scales.

We repeat the computations using a more dissipative filter. In this case, we choose a fourth order filter with $\alpha_f = 0.45$. The results are shown in figure 22. We observe that the vortical structures along the contact discontinuities are greatly attenuated.

The PAD and NAD detectors work as expected, being activated around shock locations and not as much around contact discontinuities. A comparison of the nodes detected with PAD and NAD detectors for each of the hybrid schemes is shown in figure 23. It is shown that for this test case, for both hybrid schemes, the detectors are able to identify properly the shock locations. However, we observe that, at this time step, the most of the contact discontinuities are computed using the LDFD scheme. This behaviour is explained because of the self-steepening nature of shocks, while the contact discontinuities tend to get smeared over time.

In figure 24 we plot a zoom of the region $[0.38, 0.52] \times [0.38, 0.52]$ using the different schemes and filters. It is observed the effect of using more dissipative filters in the solution of the hybrid schemes. The central structure is similar for all the schemes, although it is seen that the hybrid schemes with the tenth order filter develop Taylor-Rayleigh instabilities along the tail of the structure. It is also seen that this structures are incipient for the CRWENO and HFDCRWENO with the fourth-order filter.
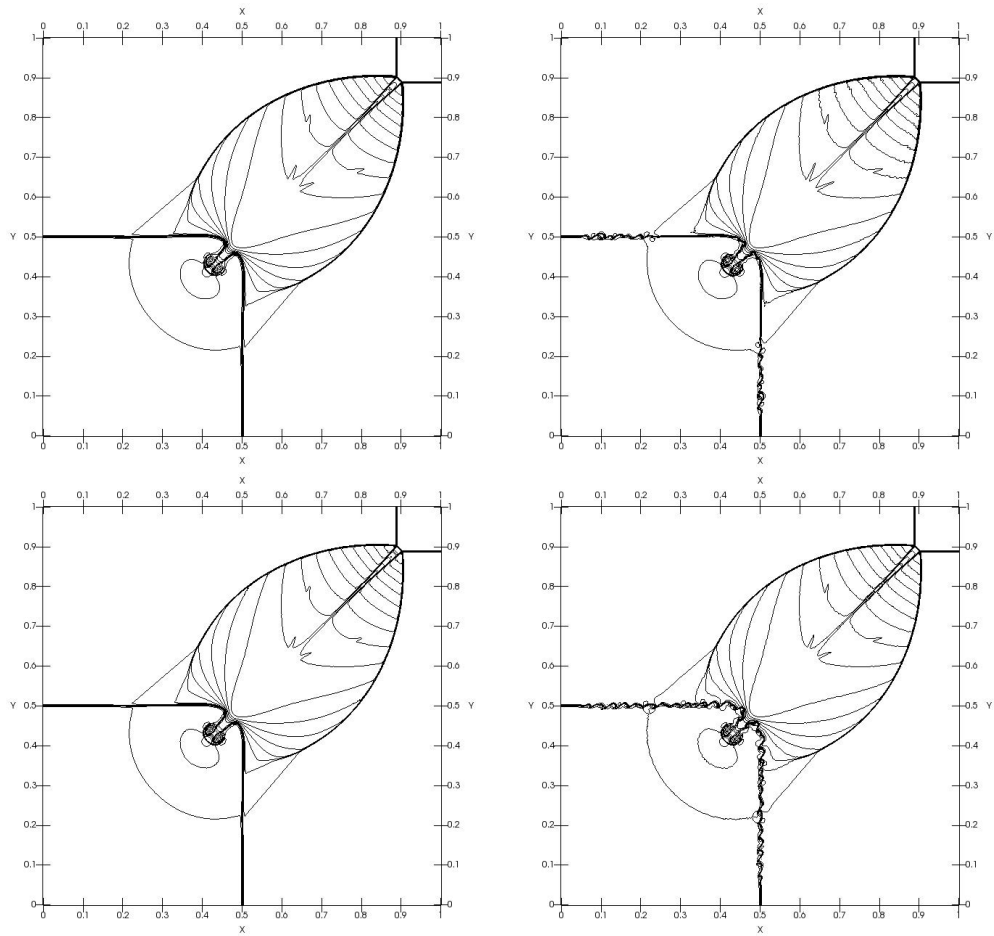
Figure 21: 2D Riemann Problem. Results obtained with WENO (top-left) and CRWENO (bottom-left) schemes compared to those of the HFDWENO (top-right)and HFDCR-WENO (bottom-right) approaches using a tenth order filter with $\alpha_f = 0.45$. We plot the results for a 800×800 mesh, with 30 equally spaced density contours between 0.54 and 1.7 at time $t = 0.25$.
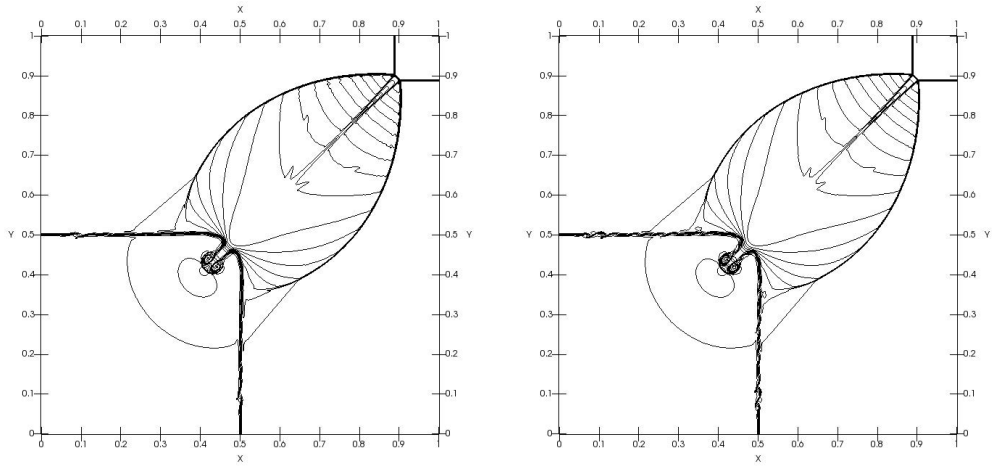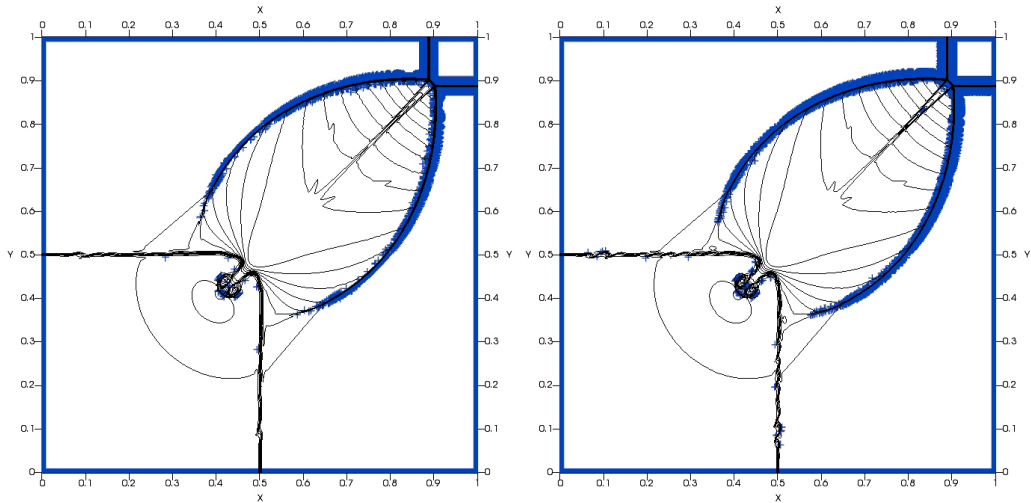
Figure 22: 2D Riemann Problem. Results obtained with the hybrid HFDWENO (left) and HFDCRWENO (right) schemes using a fourth order filter with $\alpha_f = 0.45$. We plot the results for a 800×800 mesh, with 30 equally spaced density contours between 0.54 and 1.7 at time $t = 0.25$.

Figure 23: 2D Riemann Problem. Detected points by PAD and NAD for the hybrid HFDWENO (left)and HFDCRWENO (right) schemes using a fourth order filter with $\alpha_f = 0.45$. We plot the results for a 800×800 mesh, with 30 equally spaced density contours between 0.54 and 1.7 at time $t = 0.25$.

36
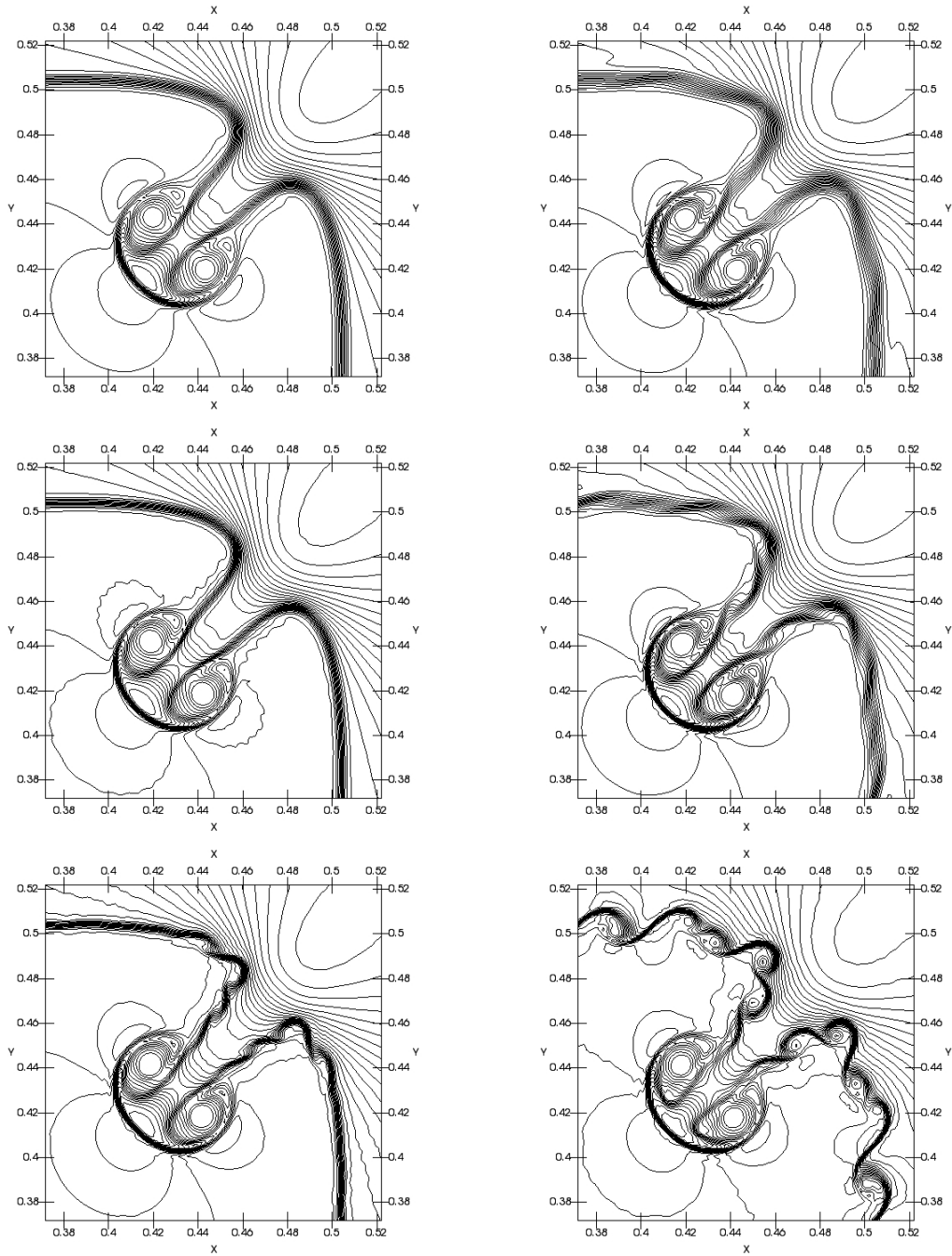
Figure 24: 2D Riemann Problem. Zoom of the region $[0.38, 0.52] \times [0.38, 0.52]$ using the WENO (top-left), HFDWENO with fourth order filter (top-right), CRWENO (middle-left), HFDCRWENO with fourth order filter (middle-right), HFDWENO with tenth order filter (bottom-left) and HFDCRWENO with tenth order filter (bottom-right) schemes. We plot the results for a 800×800 mesh, with 37 equally spaced density contours between 0.8 and 1.35 at time $t = 0.25$.

7.5. Double Mach Reflection of a Strong Shock

This two-dimensional test case is used to assess the performance of the algorithm in the presence of strong discontinuities. It was proposed by Woodward and Colella in [37] as a benchmark for Euler codes.

A Mach 10 strong shock reflects from an inviscid wall resulting in secondary shock waves and contact discontinuities.

It takes place in a $[0, 4] \times [0, 1]$ rectangular domain. The initial condition is an oblique Mach 10 shock forming 60 degrees with the X axis and intersecting the bottom boundary $(y = 0)$ at $x = 1/6$.

The flow conditions upstream and dowstream of the shock are, respectively:

$$
\begin{aligned}
(\rho_u, u_u, v_u, p_u) &= (8.000, 7.145, -4.125, 116.500) \\
(\rho_d, u_d, v_d, p_d) &= (1.400, 0.000, 0.000, 1.000)
\end{aligned}
\tag{32}
$$

The bottom boundary $(y = 0)$ is divided in two regions: the first region $(0 < x < 1/6)$ takes the upstream flow conditions, and the second region $(x \geqslant 1/6)$ is an inviscid wall.

The upper boundary $(y = 1)$ takes the analytic values of a Mach 10 oblique shock.

The left and right boundaries $(x = 0$ and $x = 4)$ are set to the up- and downstream flow conditions.

The positivity preserving technique does not activate in the present case on the WENO and HFDWENO schemes, but it gets activated quite profusely around the shock location on the first few iterations of the CRWENO and HFDCRWENO simulations. The frequency of activation decreases drastically past a few iterations, and only one or two points need the positivity correction for the rest of the simulation.

In figures 25 and 26 we present the results using the classic schemes versus the hybrid schemes using a tenth order filter with $\alpha_\mathrm{f} = 0.45$. In figure 27, the nodes detected by the PAD and NAD detectors are shown.
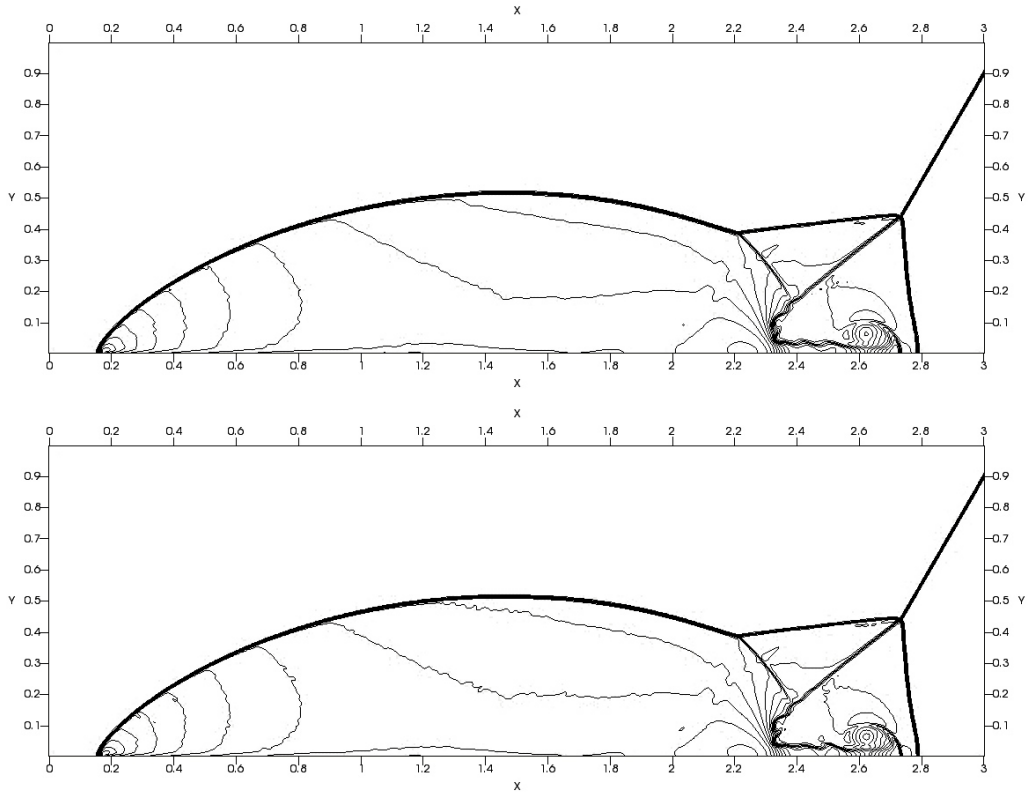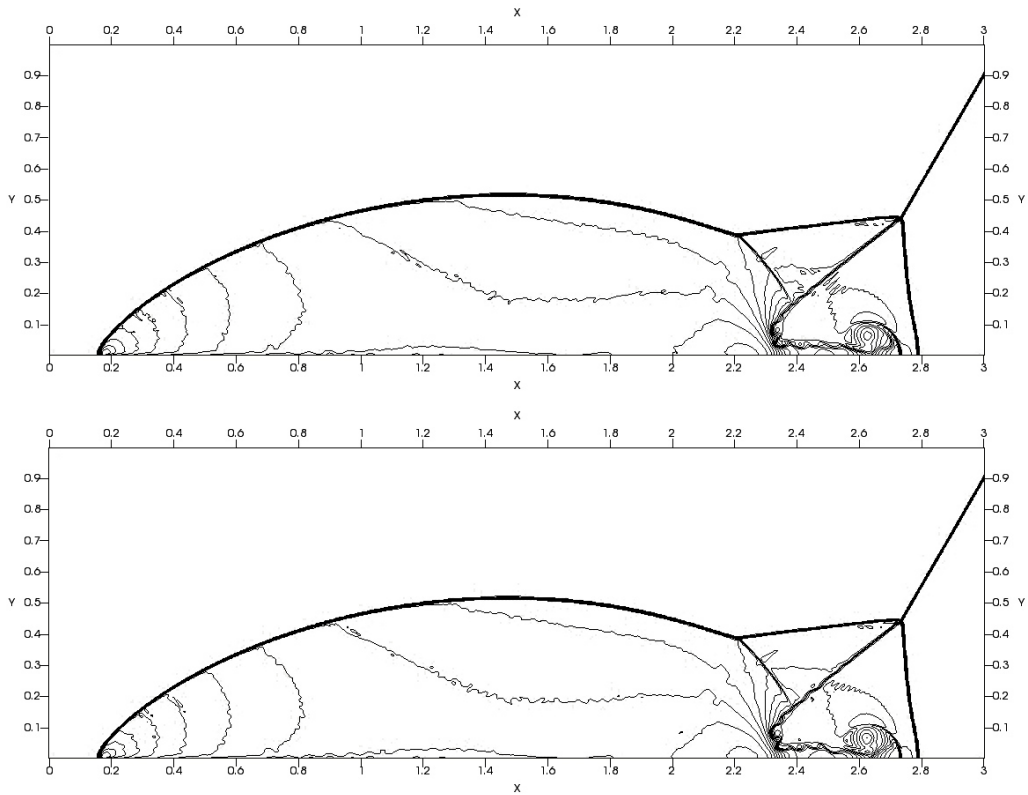
Figure 25: Double Mach Reflection of a Strong Shock. Results obtained with WENO (top) and HFDWENO (bottom) schemes. We plot the results for a 960×240 mesh using 30 equally spaced density contours between 1.731 and 20.920 at time $t = 0.2$.
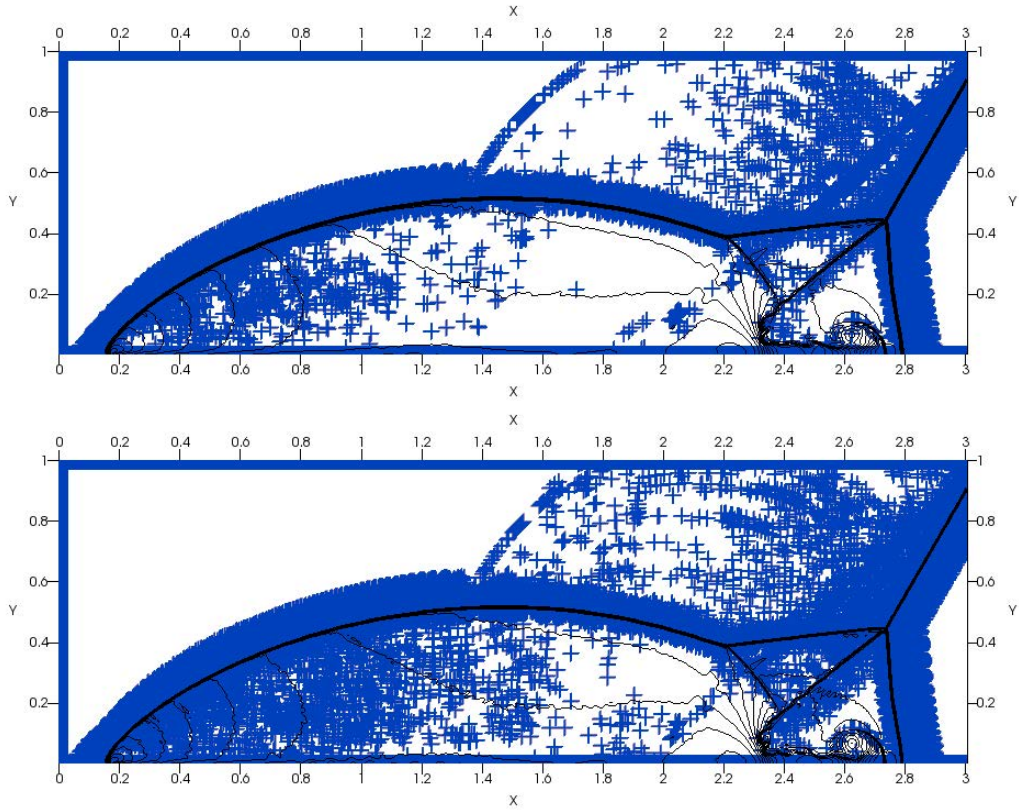
Figure 26: Double Mach Reflection of a Strong Shock. Results obtained with CRWENO (top) and HFDCRWENO (bottom) schemes. We plot the results for a 960×240 mesh using 30 equally spaced density contours between 1.731 and 20.920 at time $t = 0.2$.

Figure 27: Detected points by PAD and NAD for the hybrid HFDWENO (top) and HFDCRWENO (bottom) schemes using a tenth order filter with $\alpha_f = 0.45$. We plot the results for a 960×240 mesh using 30 equally spaced density contours between 1.731 and 20.920 at time $t = 0.2$.

In figure 28 we present a zoom of the blow-up region for all the employed schemes.
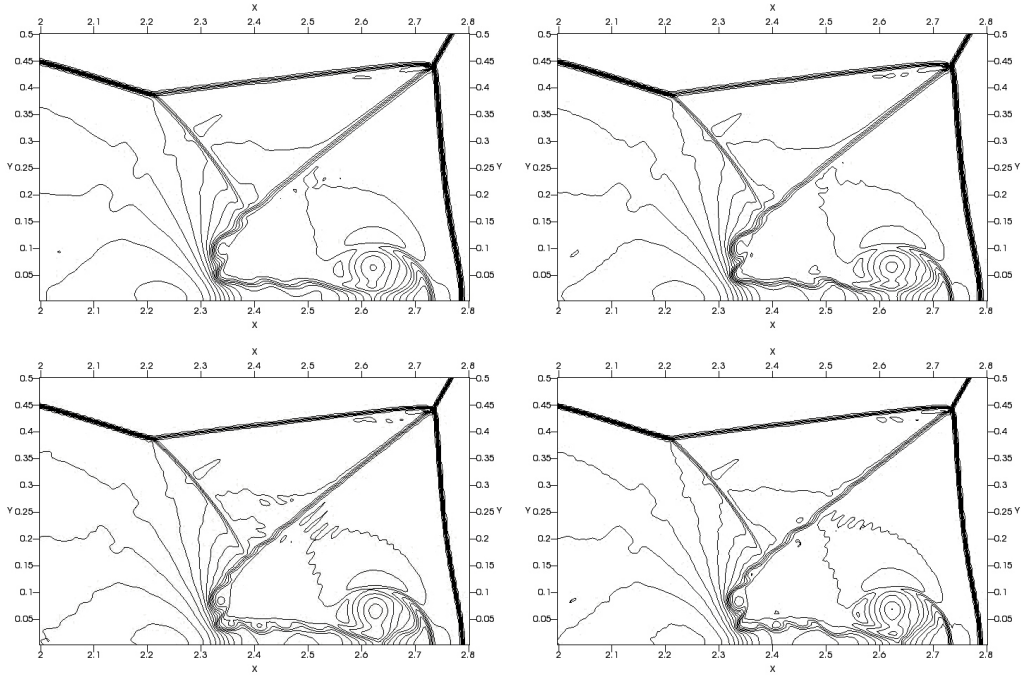
Figure 28: Blow-up region detail. 960x240 mesh. 30 equispaced density contours between 1.731 and 20.920 at time $t = 0.2$. WENO (top left), HFDWENO (top right), CRWENO (bottom left) and HFDCRWENO (bottom right).

The results obtained for the hybrid schemes are similar to those obtained for the (CR)WENO schemes. The HFDWENO scheme seems to obtain a less dissipative result than the WENO scheme, since the vortex roll-up is more pronounced. CRWENO and the HFDCRWENO obtains comparable results.

We remark the great time reduction obtained using the hybrid schemes, as shown in table 11.

Table 11: Double Mach Reflection of a Strong Shock. Time comparative

CFL=0.5	Total Time (s)		Saved Time (%)	Total Time (s)		Saved Time (%)
Mesh	WENO	HFDWENO		CRWENO	HFDCRWENO	
240x60	87.72	66.01	24.75	279.66	160.73	42.52
480x120	755.17	448.18	40.65	2315.51	1026.14	55.68
960x240	6251.02	3535.66	43.43	18929.66	5511.15	70.88
1920x480	54724.75	26938.10	50.77	164006.48	35775.47	78.18

42

7.6. Supersonic Flow Around a Cylinder

The aim of this test is to asses the ability of the proposed schemes to be applied in curvilinear grids. We study the supersonic flow around a cylinder of unitary radius with freestream Mach number $M = 3.0$. We take the stand-off distance normalized by the diameter of the cylinder and the normalized stagnation pressure p_0 as the reference parameters for this case [35].

A sketch of the mesh configuration, boundary conditions and definition of stand-off distance and stagnation point is shown in figure 29. The mesh is constructed with 100 divisions in the radial direction and 100 in the circumferential direction, so both families of lines are orthogonal to each other. This property makes it easier to impose the inviscid wall boundary condition at $R = 1$. At $R = R_{\text{ext}} = 5R$ supersonic inflow boundary condition is imposed. Supersonic outflow condition is imposed on the rest of the domain. This particular value of R_{ext} is chosen so that the boundaries are sufficiently far away from the shock location. The simulation is run until all schemes have fully converged to the stationary state, using a fourth-order filter with $\alpha_{\text{f}} = 0.45$.
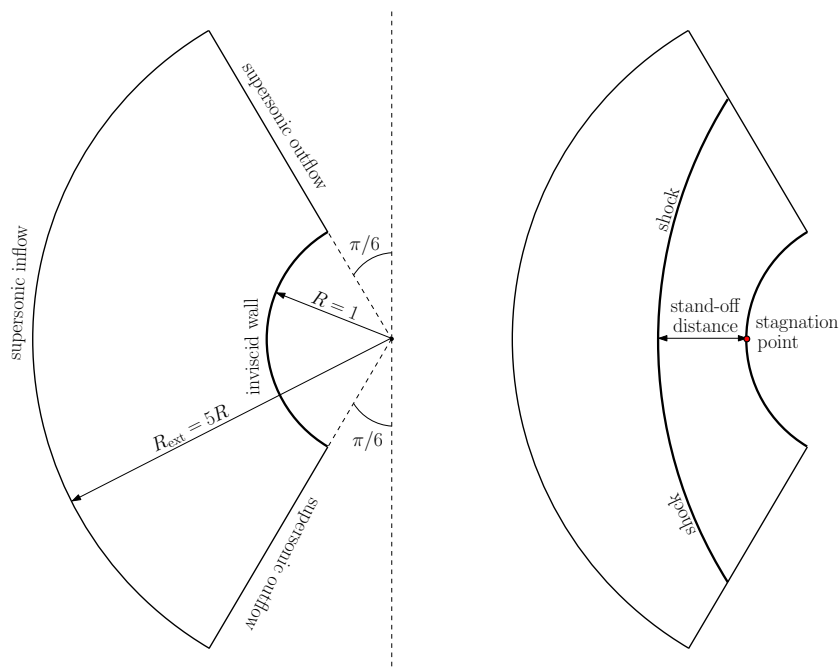

Figure 29: Test case definition and boundary conditions (left). Schematic drawing of the location of the stagnation point and definition of the stand-off distance (right).

The positivity preserving technique does not get activated for any of the studied schemes in the present test case.

In figure 30 the pressure contours of the solution are presented for the studied hybrid schemes.
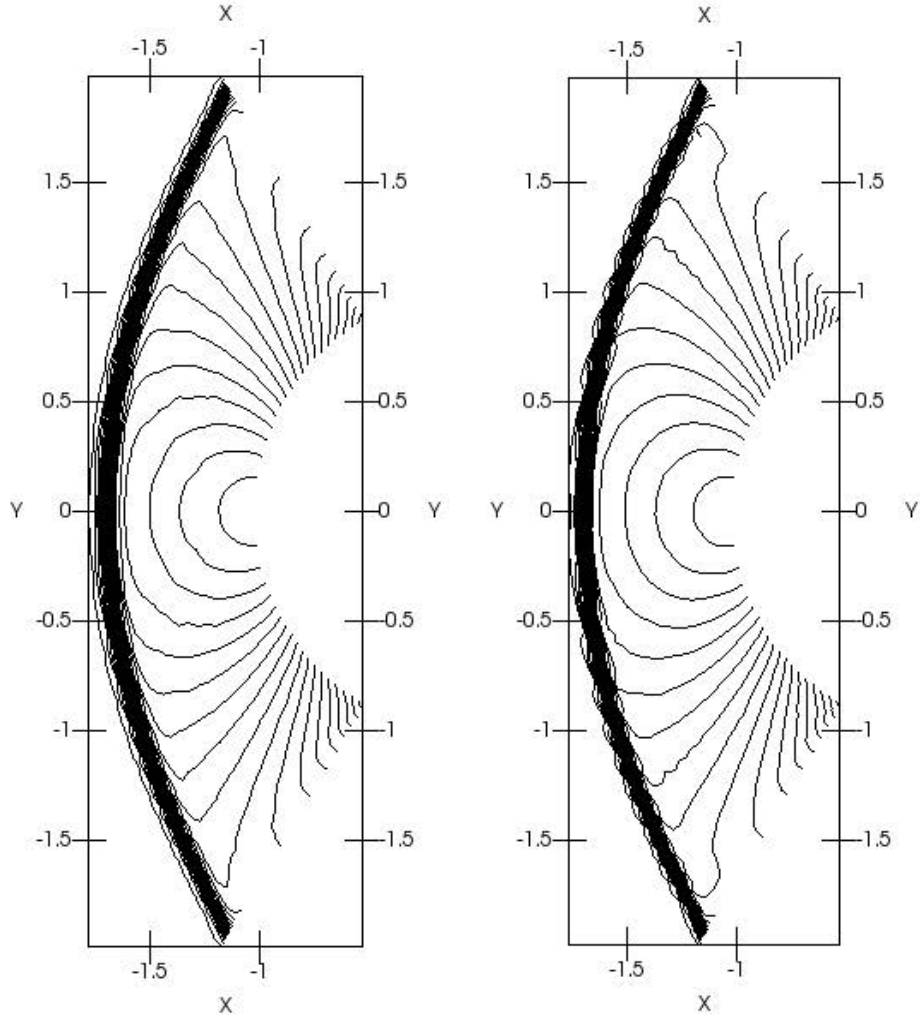

Figure 30: Supersonic Flow Around a Cylinder test case. Results using the hybrid HFDWENO (left) and HFDCRWENO (right) schemes using a fourth-order filter with $\alpha_{\mathrm{f}} = 0.45$. We plot the results for a 100×100 mesh using 25 equally spaced density contours between 0.5 and 9.

In table 12 we present a comparative of the results for the stagnation

pressure and stand-off distance using the different hybrid and (CR)WENO schemes. The results obtained by the hybrid schemes are similar to those obtained for the (CR)WENO schemes.

Table 12: Resulting parameters for the Supersonic Flow Around a Cylinder test case.

Scheme	p_0/p_∞	Stand-off distance / D
WENO	12.003	0.388
HFDWENO	12.001	0.387
CRWENO	12.017	0.402
HFDCRWENO	12.023	0.398
Reference sol. [43]	12.061	—

7.7. Mach 3 Tunnel with a Step

This case will be used as a validation of the MLS communication technique between grids in the presence of shocks. In order to compare the results obtained here with those by Woodward and Colella [37], we employed the same treatment for the expansion corner, following the implementation indicated in [44].
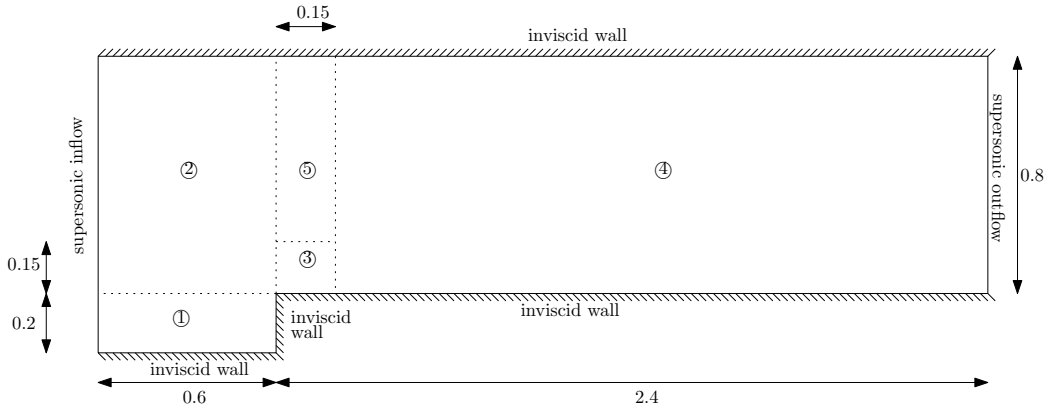

Figure 31: Mach 3 Tunnel with a Step. Initial setup and mesh decomposition.

In figure 31 the initial setup of the problem is exposed. A cubic polynomial basis is employed as initial guess for the MLS reconstruction. The simulation is run until $t = 4.0$.

Two different configurations of meshes are tested, namely:

$$
A \begin{cases} \text{Mesh 1:} & 90 \times 32 \\ \text{Mesh 2:} & 105 \times 120 \\ \text{Mesh 3:} & 24 \times 24 \\ \text{Mesh 4:} & 360 \times 128 \\ \text{Mesh 5:} & 24 \times 104 \end{cases} \qquad B \begin{cases} \text{Mesh 1:} & 120 \times 80 \\ \text{Mesh 2:} & 120 \times 320 \\ \text{Mesh 3:} & 30 \times 30 \\ \text{Mesh 4:} & 450 \times 320 \\ \text{Mesh 5:} & 30 \times 290 \end{cases}
$$

In configuration A, the meshes labeled as 1 and 2 are non-conforming with each other, mesh 2 is not conforming with meshes 3 and 5, and meshes 3, 4 and 5 are conforming. With this mesh placement, the MLS approximation for communication between meshes is put to the test.

We use a tenth-order filter with $\alpha_f = 0.45$. The positivity preserving technique does not activate in the present case for the HFDWENO scheme on neither of the studied configurations. The activation for the HFDCRWENO scheme is very scarce and it happens around $x = 0.6$ where the upper shock meets the upper wall.

In figure 32, we present the results obtained with the hybrid schemes using the configuration A. Both hybrid methods agree well with the solutions provided in [37] and [44] for a single 480x160 mesh, which is a grid with an equivalent resolution to that of configuration A.
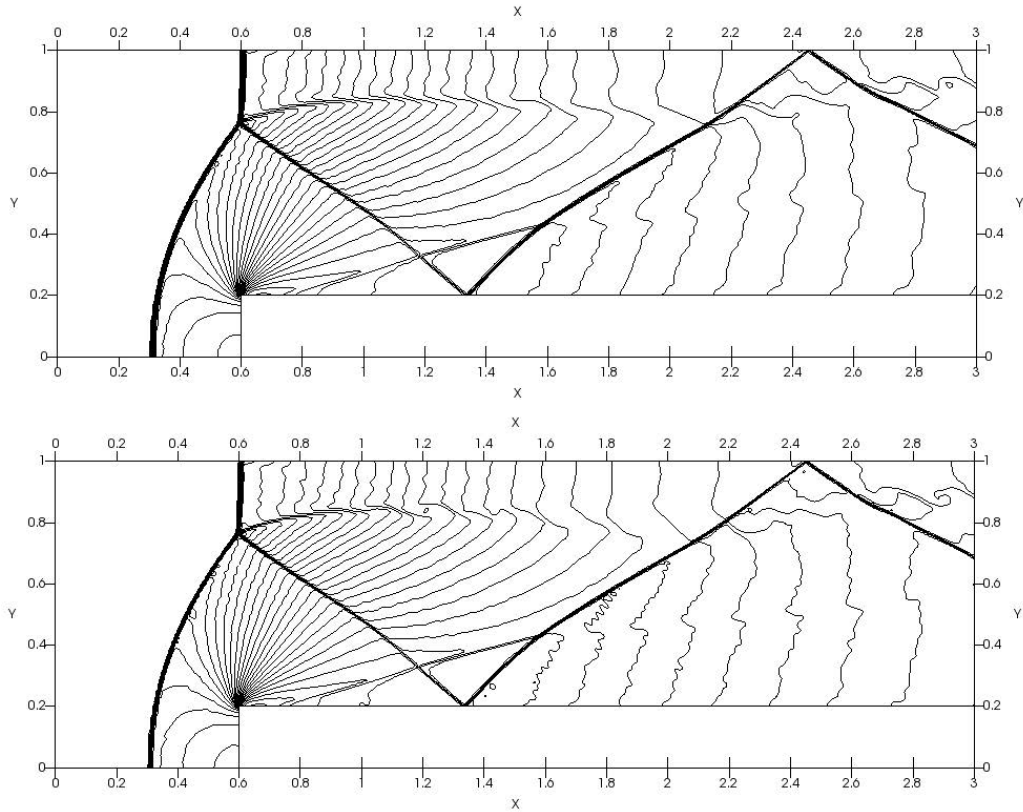
Figure 32: Mach 3 Tunnel with a Step. Results obtained with HFDWENO (top) and HFDCRWENO (bottom) for configuration A. We plot 30 equally spaced density contours between 0.257 and 6.607.

In configuration B, although all the meshes are conforming to one another, the MLS procedure is still employed. The aim of this finer configuration is to assess the correct capturing and treatment of the Kelvin-Helmholtz instability that forms around $y = 0.8$ for $x \geqslant 0.6$. Figure 33 shows that the hybrid schemes with the multi-block MLS method are able to accurately capture the Kelvin-Helmholtz instability. Moreover, we remark that the use of the proposed MLS procedure for multi-block grids does not introduce any kind of perturbations or alterations in the overall scheme in none of the configurations.
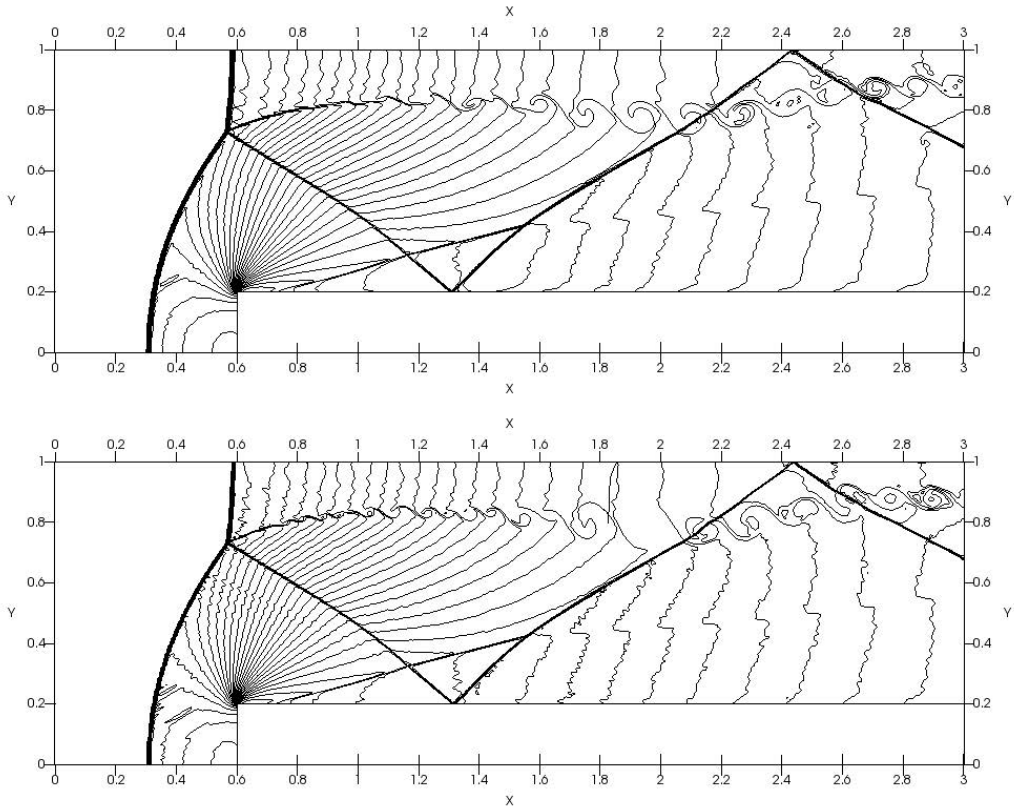
Figure 33: Mach 3 Tunnel with a Step. Results obtained with HFDWENO (top) and HFDCRWENO (bottom) for configuration A. We plot 30 equally spaced density contours between 0.32 and 6.15.

7.8. Inviscid Strong Vortex-Shock Wave Interaction

This is a two-dimensional unsteady inviscid flow including multiple shock discontinuities. This case is proposed in the 5th International Workshop on High-Order CFD Methods (HiOCFD5) [45]. The initial setup is presented in figure 34.
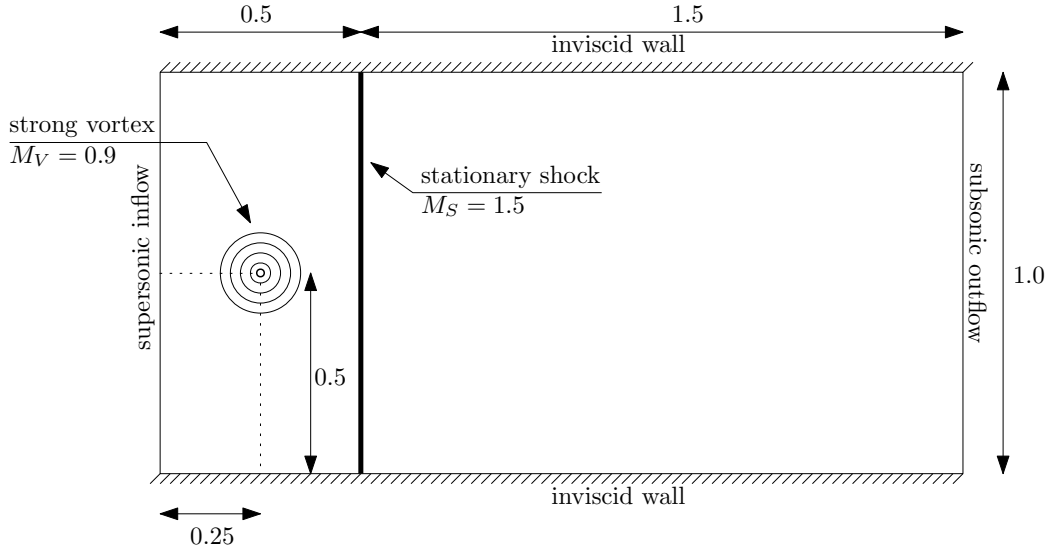
Figure 34: Inviscid Strong Vortex-Shock Wave Interaction. Initial setup

There is a stationary shock with Mach number $M_S = 1.5$ located at $x = 0.5$. The center of the vortex is located at $(x_c, y_c) = (0.25, 0.5)$ and the upstream conditions (everywhere left of the shock except within the vortical region) are given by:

$$(\rho_u, u_u, v_u, p_u) = (1.0, M_S\sqrt{\gamma}, 0.0, 1.0) \tag{33}$$

The downstream flow quantities (ρ_d, u_d, v_d, p_d) are determined using the stationary shock conditions and the upstream values of the flow.

$$
\begin{aligned}
\rho_d &= \rho_u \frac{(\gamma + 1) M_S^2}{2 + M_S^2 (\gamma - 1)} \\
u_d &= u_u \frac{2 + (\gamma - 1) M_S^2}{M_S^2 (\gamma + 1)} \\
v_d &= v_u \\
p_d &= p_u \left(1 + \frac{2\gamma (M_S^2 - 1)}{\gamma + 1} \right)
\end{aligned}
\tag{34}
$$

The vortex rotates counter-clockwise with angular velocity v_θ expressed

49

as:

$$
v_\theta(r) = \begin{cases}
v_\mathrm{m}\dfrac{r}{a} & \text{if} \quad r \leqslant a \\[2ex]
v_\mathrm{m}\dfrac{a}{a^2 - b^2}\left(r - \dfrac{b^2}{r}\right) & \text{if} \quad a \leqslant r \leqslant b \\[2ex]
0 & \text{if} \quad r > b
\end{cases} \tag{35}
$$

where $r = \sqrt{(x - x_c)^2 + (y - y_c)^2}$ is the distance from the vortex center, $a = 0.075$ and $b = 0.175$. v_m is the maximum angular velocity, occurring at $r = a$. The ratio $M_\mathrm{V} = v_\mathrm{m}/\sqrt{\gamma}$ is taken as a measure of the vortex strength, in this case $M_\mathrm{V} = 0.7$.

The superimposition of the vortex can be regarded as a perturbation added to the previously calculated upstream values of the flow. Thus, in the vortical region we have:

$$
\begin{aligned}
u_\mathrm{vor}(r) &= u_u - \frac{v_\mathrm{m}r}{a}\frac{y - y_c}{r} \\[2ex]
v_\mathrm{vor}(r) &= v_u + \frac{v_\mathrm{m}r}{a}\frac{x - x_c}{r}
\end{aligned} \tag{36}
$$

To compute the temperature field inside the vortex, the following ODE has to be integrated:

$$
\frac{dT_\mathrm{vor}(r)}{dr} = \frac{\gamma - 1}{R\gamma}\frac{v_\theta^2(r)}{r} \implies \int_r^b \frac{dT_\mathrm{vor}(r)}{dr}dr = \int_r^b \frac{\gamma - 1}{R\gamma}\frac{v_\theta^2(r)}{r}dr \tag{37}
$$

where R is the gas constant, $T_\mathrm{vor}(b) = T_u = p_u/\rho_u$. With all this data, $T_\mathrm{vor}(r)$ can be calculated.

Finally, the density and pressure inside the vortex are:

$$
\begin{aligned}
\rho_\mathrm{vor}(r) &= \rho_u\left(\frac{T_\mathrm{vor}(r)}{T_u}\right)^{\frac{1}{\gamma - 1}} \\[3ex]
p_\mathrm{vor}(r) &= p_u\left(\frac{T_\mathrm{vor}(r)}{T_u}\right)^{\frac{\gamma}{\gamma - 1}}
\end{aligned} \tag{38}
$$

We use a fourth-order filter with $\alpha_f = 0.45$. In this example, the use of the tenth-order filter gives a very noisy solution. The simulation is run until $t = 0.7$ in a 1000×500 mesh. The positivity preserving technique does not activate in the present case for any of the studied schemes.

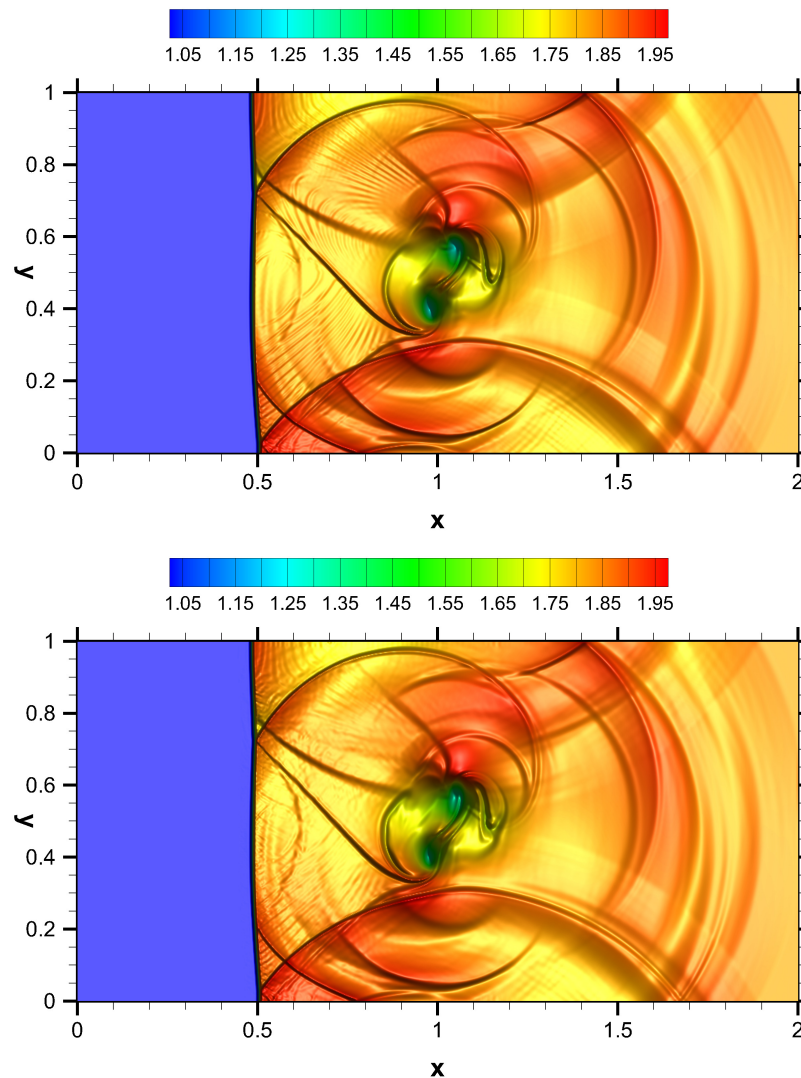In figures 35 and 36 we plot the results obtained by the hybrid and the (CR)WENO schemes.

Figure 35: Inviscid Strong Vortex-Shock Wave Interaction. Density field obtained with the WENO (top) and HFDWENO schemes (bottom).
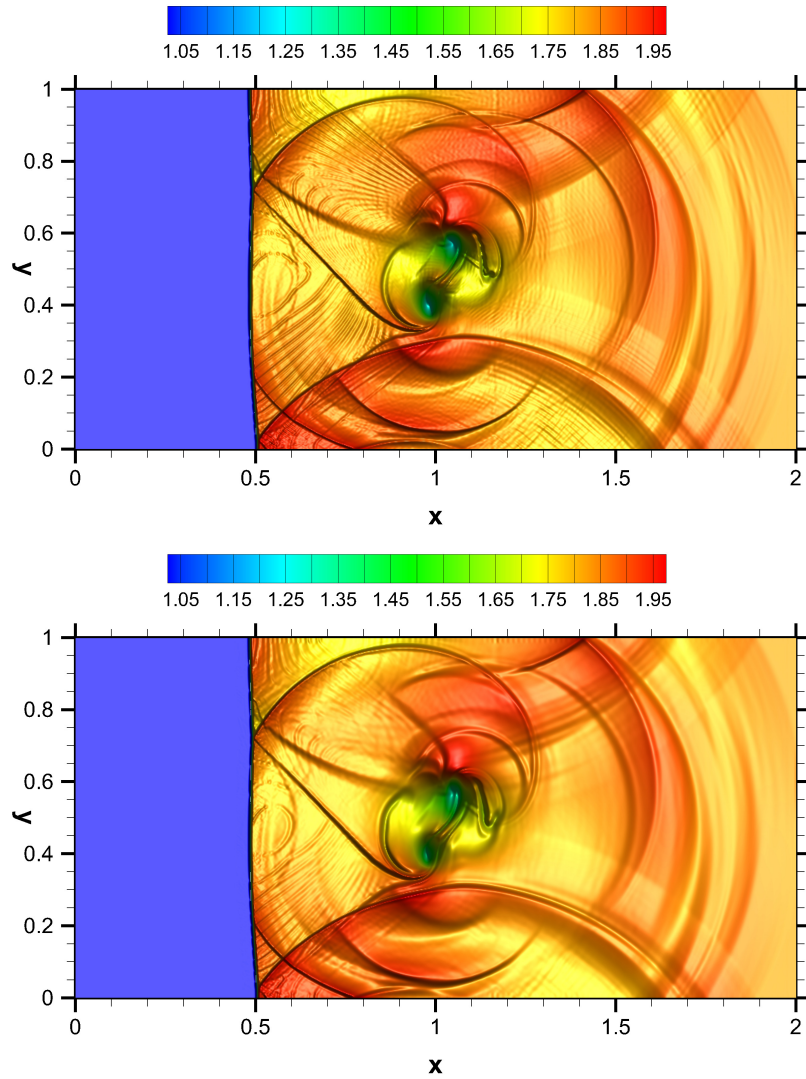
Figure 36: Inviscid Strong Vortex-Shock Wave Interaction. Density field obtained with the CRWENO (top) and HFDCRWENO schemes (bottom).

The obtained solutions are in agreement with those of [45, 46]. The HFDCRWENO obtains less dissipative results than the HFDWENO scheme as expected, and this results in a sharper definition of some of the flow structures. However, the use of the fourth-order filter causes that the solution obtained by the hybrid schemes is more dissipative. All the schemes are able to capture some important features of the flow as the vortex core splitting

and the Kelvin-Helmholtz instability along the slip layer.

In table 13, it is seen the notable differences in computational time of the different schemes.

Table 13: Inviscid Strong Vortex-Shock Wave Interaction. Time comparative

CFL=0.5	Total Time (s)		Saved Time (%)	Total Time (s)		Saved Time (%)
Mesh	WENO	HFDWENO		CRWENO	HFDCRWENO	
1000x500	18830.00	7726.27	58.96	59747.19	10701.44	82.08

8. Conclusions

A new high-order *a posteriori* hybrid finite-difference scheme has been presented. It combines the speed of explicit finite difference methods with the shock-handling capabilities of the Weighted Essentially Non-Oscillatory schemes.

The validation procedure has illustrated the ability of the algorithm to capture discontinuities accurately. The solution obtained with the hybrid methods is comparable to that of the classic schemes, but with significant time savings in both cases.

In this work we have also presented an approach based on Moving Least Squares (MLS) to apply the numerical scheme to block-structured meshes. The proposed MLS framework is proven to be a very useful tool to maintain the accuracy when passing information between Finite Difference meshes. It yields very accurate results in flows with shocks, as seen in the Mach 3 Tunnel with a Step problem.

Finally, a very challenging test case such as the Inviscid Strong Vortex-Shock Wave Interaction is run to fully test our schemes. Given the great complexity of the flow structures present in this case, the results are satisfactory because both of the schemes are able to capture the complicated flow structures this case presents.

The results presented in this work show that the proposed scheme is able to capture accurately shock waves and also the smooth structures of the flow.

Appendix A. Flux vector splitting procedure

For the WENO 5 and CRWENO 5 interpolation to work properly, given that they are upwind schemes, the flux function has to be monotone. The previous statement does not hold for a general flux function, so it is mandatory to perform a flux vector splitting (FVS). As an example, we take the flux on the $\xi-$direction, $\hat{\mathbf{F}}$.

$$\hat{\mathbf{F}}_{i+1/2} = \hat{\mathbf{F}}_i^+ + \hat{\mathbf{F}}_{i+1}^- \tag{A.1}$$

so that

$$\frac{\partial \hat{\mathbf{F}}^+}{\partial \hat{\mathbf{U}}} \geqslant 0 \text{ and } \frac{\partial \hat{\mathbf{F}}^-}{\partial \hat{\mathbf{U}}} \leqslant 0 \tag{A.2}$$

The two most common techniques to achieve this, are:

Global Lax-Friedrichs:

$$\hat{\mathbf{F}}_j^{\pm} = \frac{1}{2}(\hat{\mathbf{F}}_j \pm \alpha \hat{\mathbf{U}}_j) \quad \text{with} \quad \alpha = \max_{\hat{\mathbf{U}}} \left(\max_m \left| \lambda^{(m)} \right| \right) \tag{A.3}$$

Local Lax-Friedrichs:

$$\hat{\mathbf{F}}_j^{\pm} = \frac{1}{2}(\hat{\mathbf{F}}_j \pm \alpha_j \hat{\mathbf{U}}_j) \quad \text{with} \quad \alpha_j = \max_m \left| \lambda^{(m)} \right| \tag{A.4}$$

The main difference between A.3 and A.4 is that the α parameter, which adds dissipation to the scheme, is calculated differently. In A.3 it is calculated globally as the maximum of the absolute value of the eigenvalues on the whole or the relevant range of $\hat{\mathbf{U}}$, hence more dissipation is added in the global case when compared to the local case. In A.4 α is calculated locally as the maximum of the absolute value of the eigenvalues of the point j, using just the point for the calculation of the dissipation, ensures less dissipation is added than in the global case.

For a generalized coordinate system, please refer to [47] for the expressions of $\lambda^{(m)}$.

Appendix B. WENO 5 scheme

In this appendix the WENO 5 formulation is expounded. The flux vector splitting procedure of Appendix A, splits the flux into a positive and a negative part. The formulation will only be explained for the positive part, being the other part analogous.

As suggested in [11], the characteristic formulation is more robust when dealing with problems involving strong shocks. The projection of the calculated split flux into the characteristic space is done as follows:

$$\mathcal{F}^+_{p,m} = l_{i+1/2,m} \hat{\mathbf{F}}^+_p \qquad p = i - 2, \ldots, i + 2 \qquad \text{B.1}$$

where $\mathcal{F}^+_{p,m}$ denotes the mth characteristic variable of the positive part of the flux, and $l_{i+1/2,m}$ denotes the mth left eigenvector of the Jacobian matrix $\dfrac{\partial \hat{\mathbf{F}}}{\partial \hat{\mathbf{U}}}$, computed at $i + 1/2$ using the Roe-averaged values that can be found in [48]. Explicit expressions in general coordinates for the eigenvalue matrix and left and right eigenvectors matrices can be found in [49].

We can write the interface flux reconstruction $\mathcal{F}^+_{i+1/2,m}$ as:

$$\mathcal{F}^+_{i+1/2,m} = \omega^1_{i,m} \mathcal{F}^{+,1}_{i+1/2,m} + \omega^2_{i,m} \mathcal{F}^{+,2}_{i+1/2,m} + \omega^3_{i,m} \mathcal{F}^{+,3}_{i+1/2,m} \qquad \text{B.2}$$

where $\mathcal{F}^{+,k}_{i+1/2,m}$ stands for the kth candidate polynomial, and $\omega^k_{i,m}$ stands for its corresponding nonlinear weight.

The expressions for the candidate polynomials are:

$$\mathcal{F}^{+,1}_{i+1/2,m} = \frac{2}{6} \mathcal{F}^+_{i-2,m} - \frac{7}{6} \mathcal{F}^+_{i-1,m} + \frac{11}{6} \mathcal{F}^+_{i,m}$$

$$\mathcal{F}^{+,2}_{i+1/2,m} = \frac{-1}{6} \mathcal{F}^+_{i-1,m} + \frac{5}{6} \mathcal{F}^+_{i,m} + \frac{2}{6} \mathcal{F}^+_{i+1,m} \qquad \text{B.3}$$

$$\mathcal{F}^{+,3}_{i+1/2,m} = \frac{2}{6} \mathcal{F}^+_{i,m} + \frac{5}{6} \mathcal{F}^+_{i+1,m} - \frac{1}{6} \mathcal{F}^+_{i+2,m}$$

There exists optimal weights d_k such that if $\omega^k_{i,m} = d_k \forall k$ the resulting interpolation is of fifth order. The WENO 5 optimal weights are:

$$d_1 = 1/10 \qquad d_2 = 3/10 \qquad d_3 = 6/10 \qquad \text{B.4}$$

The WENO limiting causes the nonlinear weights to converge to their optimal value where the solution is smooth, whereas if the solution has a discontinuity, the weight of the corresponding stencil approaches zero to yield a non oscillatory flux interpolation. This can be achieved with the aid of smoothness indicators $\beta_{i,m}^k$ that serve the purpose of scaling the optimal weights. They are defined as:

$$\beta_{i,m}^1 = \frac{13}{2} \left(\mathcal{F}_{i-2,m}^+ - 2\mathcal{F}_{i-1,m}^+ + \mathcal{F}_{i,m}^+ \right)^2 + \frac{1}{4} \left(\mathcal{F}_{i-2,m}^+ - 4\mathcal{F}_{i-1,m}^+ + 3\mathcal{F}_{i,m}^+ \right)^2$$

$$\beta_{i,m}^2 = \frac{13}{2} \left(\mathcal{F}_{i-1,m}^+ - 2\mathcal{F}_{i,m}^+ + \mathcal{F}_{i+1,m}^+ \right)^2 + \frac{1}{4} \left(\mathcal{F}_{i-1,m}^+ - \mathcal{F}_{i+1,m}^+ \right)^2 \qquad \text{B.5}$$

$$\beta_{i,m}^3 = \frac{13}{2} \left(\mathcal{F}_{i,m}^+ - 2\mathcal{F}_{i+1,m}^+ + \mathcal{F}_{i+2,m}^+ \right)^2 + \frac{1}{4} \left(3\mathcal{F}_{i,m}^+ - 4\mathcal{F}_{i+1,m}^+ + \mathcal{F}_{i+2,m}^+ \right)^2$$

$$\alpha_{i,m}^k = \frac{d_k}{(\beta_{i,m}^k + \varepsilon)^q} \qquad k = 1, 2, 3 \qquad \text{B.6}$$

where ε is a small number to avoid division by zero (usually is picked as 10^{-6}), and q ensures that the non-smooth stencil weights approach zero fast enough. It usually has the value of $q = 2$.

To guarantee convexity, the weights α_k are normalized as:

$$\omega_{i,m}^k = \frac{\alpha_{i,m}^k}{\displaystyle\sum_{s=1}^{3} \alpha_{s,m}^k} \qquad k = 1, 2, 3 \qquad \text{B.7}$$

The above weights are excessively dissipative and following the recommendation of [23] we map the weights with the following function, that causes the weights to converge faster to their optimal values:

$$g_k(\omega) = \frac{\omega \left(d_k + d_k^2 - 3d_k\omega + \omega^2 \right)}{d_k^2 + \omega(1 - 2d_k)} \qquad k = 1, 2, 3 \qquad \text{B.8}$$

The new mapped weights, denoted with a hat, are given by:

$$\hat{\alpha}_{i,m}^k = g_k(\omega_k) = \frac{\omega_k \left(d_k + d_k^2 - 3d_k\omega_k + \omega_k^2 \right)}{d_k^2 + \omega_k(1 - 2d_k)} \qquad k = 1, 2, 3 \qquad \text{B.9}$$

Finally, the mapped weights are normalized in the same fashion as B.7

$$\hat{\omega}_{i,m}^k = \frac{\hat{\alpha}_{i,m}^k}{\displaystyle\sum_{s=1}^{3}\hat{\alpha}_{i,m}^s} \qquad k = 1,2,3 \qquad\qquad \text{B.10}$$

To sum up, the final form of the WENO 5 interface interpolation, with mapped weights, is:

$$\mathcal{F}_{i+1/2,m}^+ = \hat{\omega}_{i,m}^1 \mathcal{F}_{i+1/2,m}^{+,1} + \hat{\omega}_{i,m}^2 \mathcal{F}_{i+1/2,m}^{+,2} + \hat{\omega}_{i,m}^3 \mathcal{F}_{i+1/2,m}^{+,3} \qquad\qquad \text{B.11}$$

Afterwards, the $\mathcal{F}_{i+1/2,m}^+$ is transformed back into the conservative form using the right eigenvectors matrix as:

$$\hat{\mathbf{F}}_{i+1/2,j}^+ = \sum_m \mathcal{F}_{i+1/2,m}^+ r_{i+1/2,m} \qquad\qquad \text{B.12}$$

where $r_{i+1/2,m}$ denotes the mth right eigenvector of the Jacobian matrix $\dfrac{\partial \hat{\mathbf{F}}}{\partial \hat{\mathbf{U}}}$, computed at $i + 1/2$ using the Roe-averaged values that can be found in [48]. As said earlier, please refer to [49] for explicit expressions in general coordinates.

Appendix C. CRWENO 5 scheme

As the WENO 5, the CRWENO 5 is also formulated as a weighted sum of low-order stencils, but in this case the interpolations are compact. The characteristic form of the CRWENO 5 is implemented, but for brevity and clarity of exposition, only the component-wise version will be explained. Using the same notation as above, the candidate stencils are:

$$\frac{2}{3}\hat{\mathbf{F}}_{i-1/2}^{+,1} + \frac{1}{3}\hat{\mathbf{F}}_{i+1/2}^{+,1} = \frac{1}{6}\left(\hat{\mathbf{F}}_{i-1}^{+,1} + 5\hat{\mathbf{F}}_i^{+,1}\right)$$

$$\frac{1}{3}\hat{\mathbf{F}}_{i-1/2}^{+,1} + \frac{2}{3}\hat{\mathbf{F}}_{i+1/2}^{+,1} = \frac{1}{6}\left(5\hat{\mathbf{F}}_i^{+,1} + \hat{\mathbf{F}}_{i+1}^{+,1}\right) \qquad\qquad \text{C.1}$$

$$\frac{2}{3}\hat{\mathbf{F}}_{i+1/2}^{+,1} + \frac{1}{3}\hat{\mathbf{F}}_{i+3/2}^{+,1} = \frac{1}{6}\left(\hat{\mathbf{F}}_i^{+,1} + 5\hat{\mathbf{F}}_{i+1}^{+,1}\right)$$

The CRWENO 5 optimal weights are:

$$d_1 = 2/10 \qquad d_2 = 5/10 \qquad d_3 = 3/10 \qquad\qquad \text{C.2}$$

For the calculation of the nonlinear weights, the process is the same as in the WENO 5, where equations B.6 through B.10 are used. The smoothness indicators of equation B.5 are used as well.

Multiplying each of the equations in C.2 by its corresponding weight $\hat{\omega}_i^k$ yields an implicit system of equations:

$$\left(\frac{2}{3}\hat{\omega}_i^1 + \frac{1}{3}\hat{\omega}_i^2\right)\hat{\mathbf{F}}_{i-1/2}^+ + \left[\frac{1}{3}\hat{\omega}_i^1 + \frac{2}{3}\left(\hat{\omega}_i^2 + \hat{\omega}_i^3\right)\right]\hat{\mathbf{F}}_{i+1/2}^+ + \frac{1}{3}\hat{\omega}_i^3\hat{\mathbf{F}}_{i+3/2}^+ =$$
$$= \frac{\hat{\omega}_i^1}{6}\hat{\mathbf{F}}_{i-1}^+ + \frac{5\left(\hat{\omega}_i^1 + \hat{\omega}_i^2\right) + \hat{\omega}_i^3}{6}\hat{\mathbf{F}}_i^+ + \frac{\hat{\omega}_i^2 + 5\hat{\omega}_i^3}{6}\hat{\mathbf{F}}_{i+1}^+ \qquad \text{C.3}$$

If the characteristic version of the scheme is needed, the same procedure as in equation B.1 is used, yielding a 4-by-4 block tridiagonal system of equations.

To be able to solve this system, if non-periodic boundary conditions apply, the first and last interfaces need to be reconstructed with the non-compact WENO 5 in order to have the same number of equations and unknowns, in the style of equation B.11.

After solving the block tridiagonal system, there is no need to use equation B.12, because the obtained values are already in the conservative variable space.

For a more detailed description of the algorithm, please refer to [10].

References

[1] B. Costa, W. S. Don, High order hybrid central—WENO finite difference scheme for conservation laws, Journal of Computational and Applied Mathematics 204 (2) (2007) 209–218. doi:10.1016/j.cam.2006.01.039.

[2] S. Pirozzoli, Conservative hybrid compact-WENO schemes for shock-turbulence interaction, Journal of Computational Physics 178 (1) (2002) 81–117. doi:10.1006/jcph.2002.7021.

[3] X. Hu, B. Wang, N. Adams, An efficient low-dissipation hybrid weighted essentially non-oscillatory scheme, Journal of Computational Physics 301 (2015) 415–424. doi:10.1016/j.jcp.2015.08.043.

[4] S. Clain, S. Diot, R. Loubère, A high-order finite volume method for systems of conservation laws—multi-dimensional optimal order detection (MOOD), Journal of Computational Physics 230 (10) (2011) 4028–4050. doi:10.1016/j.jcp.2011.02.026.

[5] S. Diot, S. Clain, R. Loubère, Improved detection criteria for the multi-dimensional optimal order detection (MOOD) on unstructured meshes with very high-order polynomials, Computers & Fluids 64 (2012) 43–63. doi:10.1016/j.compfluid.2012.05.004.

[6] M. Vinokur, Conservation equations of gasdynamics in curvilinear coordinate systems, Journal of Computational Physics 14 (2) (1974) 105–125. doi:10.1016/0021-9991(74)90008-4.

[7] M. R. Visbal, D. V. Gaitonde, On the use of higher-order finite-difference schemes on curvilinear and deforming meshes, Journal of Computational Physics 181 (1) (2002) 155–185. doi:10.1006/jcph.2002.7117.

[8] M. R. Visbal, D. V. Gaitonde, High-order-accurate methods for complex unsteady subsonic flows, AIAA Journal 37 (10) (1999) 1231–1239. doi:10.2514/2.591.

[9] K. A. Hoffmann, S. T. Chiang, Computational Fluid Dynamics (Vol. 1), Engineering Education System, 2000.

[10] D. Ghosh, J. D. Baeder, Compact reconstruction schemes with weighted ENO limiting for hyperbolic conservation laws, SIAM Journal on Scientific Computing 34 (3) (2012) A1678–A1706. doi:10.1137/110857659.

[11] G.-S. Jiang, C.-W. Shu, Efficient implementation of weighted ENO schemes, Journal of Computational Physics 126 (1) (1996) 202–228. doi:10.1006/jcph.1996.0130.

[12] C. Bogey, C. Bailly, A family of low dispersive and low dissipative explicit schemes for computing aerodynamic noise, in: 8th AIAA/CEAS Aeroacoustics Conference Exhibit, American Institute of Aeronautics and Astronautics, 2002. doi:10.2514/6.2002-2509.

[13] M. R. Visbal, D. V. Gaitonde, High-order schemes for navier-stokes equations: Algorithm and implementation into fdl3di, Tech. rep., Air Force Research Lab Wright-Patterson, Air Vehicles Directorate (1998).

[14] M. Visbal, D. Gaitonde, Shock capturing using compact-differencing-based methods, in: 43rd AIAA Aerospace Sciences Meeting and Exhibit, American Institute of Aeronautics and Astronautics, 2005. `doi:10.2514/6.2005-1265`.

[15] S.-C. Lo, G. A. Blaisdell, A. S. Lyrintzis, High-order shock capturing schemes for turbulence calculations, International Journal for Numerical Methods in Fluids (2009) n/a–n/a`doi:10.1002/fld.2021`.

[16] A. Harten, The artificial compression method for computation of shocks and contact discontinuities: Iii. self-adjusting hybrid schemes, Mathematics of Computation 32 (142) (1978) 363–389.

[17] H. Yee, B. Sjgreen, Development of low dissipative high order filter schemes for multiscale navierstokes/mhd systems, Journal of Computational Physics 225 (1) (2007) 910 – 934. `doi:https://doi.org/10.1016/j.jcp.2007.01.012`.

[18] H. Yee, B. Sjgreen, Recent developments in accuracy and stability improvement of nonlinear filter methods for dns and les of compressible flows, Computers & Fluids`doi:https://doi.org/10.1016/j.compfluid.2017.08.028`.

[19] A. W. Cook, W. H. Cabot, A high-wavenumber viscosity for high-resolution numerical methods, Journal of Computational Physics 195 (2) (2004) 594–601. `doi:10.1016/j.jcp.2003.10.012`.

[20] B. Fiorina, S. Lele, An artificial nonlinear diffusivity method for supersonic reacting flows with shocks, Journal of Computational Physics 222 (1) (2007) 246–264. `doi:10.1016/j.jcp.2006.07.020`.

[21] N. Adams, K. Shariff, A high-resolution hybrid compact-ENO scheme for shock-turbulence interaction problems, Journal of Computational Physics 127 (1) (1996) 27–51. `doi:10.1006/jcph.1996.0156`.

[22] E. Johnsen, J. Larsson, A. V. Bhagatwala, W. H. Cabot, P. Moin, B. J. Olson, P. S. Rawat, S. K. Shankar, B. Sjgreen, H. Yee, X. Zhong, S. K. Lele, Assessment of high-resolution methods for numerical simulations of compressible turbulence with shock waves, Journal of Computational Physics 229 (4) (2010) 1213–1237. `doi:10.1016/j.jcp.2009.10.028`.

[23] A. K. Henrick, T. D. Aslam, J. M. Powers, Mapped weighted essentially non-oscillatory schemes: Achieving optimal order near critical points, Journal of Computational Physics 207 (2) (2005) 542–567. `doi:10.1016/j.jcp.2005.01.023`.

[24] M. Dumbser, O. Zanotti, R. Loubère, S. Diot, A posteriori subcell limiting of the discontinuous galerkin finite element method for hyperbolic conservation laws, Journal of Computational Physics 278 (2014) 47–75. doi:10.1016/j.jcp.2014.08.009.

[25] X. Nogueira, L. Ramírez, S. Clain, R. Loubère, L. Cueto-Felgueroso, I. Colominas, High-accurate sph method with multidimensional optimal order detection limiting, Computer Methods in Applied Mechanics and Engineering 310 (2016) 134–155. doi:10.1016/j.cma.2016.06.032.

[26] J. Figueiredo, S. Clain, Second-order finite volume mood method for the shallow water with dry/wet interface, SYMCOMP 2015.

[27] F. Daude, J. Berland, T. Emmert, P. Lafon, F. Crouzet, C. Bailly, A high-order finite-difference algorithm for direct computation of aerodynamic sound, Computers & Fluids 61 (2012) 46–63. doi:10.1016/j.compfluid.2011.08.017.

[28] S. F. Davis, Shock capturing with padé methods, Applied Mathematics and Computation 89 (1-3) (1998) 85–98. doi:https://doi.org/10.1016/S0096-3003(97)81649-9.

[29] X. Y. Hu, N. A. Adams, C.-W. Shu, Positivity-preserving flux limiters for high-order conservative schemes, Journal of Computational Physics 242 (2013) 169–180. doi:10.1016/j.jcp.2013.01.024.

[30] D. Whitfield, Three-dimensional unsteady euler equations solution using flux vector splitting, in: 17th Fluid Dynamics, Plasma Dynamics, and Lasers Conference, American Institute of Aeronautics and Astronautics, 1984. doi:10.2514/6.1984-1552.

[31] L. Ramírez, X. Nogueira, S. Khelladi, J.-C. Chassaing, I. Colominas, A new higher-order finite volume method based on moving least squares for the resolution of the incompressible navier–stokes equations on unstructured grids, Computer Methods in Applied Mechanics and Engineering 278 (2014) 883–901. doi:10.1016/j.cma.2014.06.028.

[32] L. Ramírez, X. Nogueira, P. Ouro, F. Navarrina, S. Khelladi, I. Colominas, A higher-order chimera method for finite volume schemes, Archives of Computational Methods in Engineering (2017) . doi:10.1007/s11831-017-9213-8.

[33] P. Lancaster, K. Salkauskas, Surfaces generated by moving least squares methods, Mathematics of Computation 37 (155) (1981) 141–141. doi:10.1090/s0025-5718-1981-0616367-1.

[34] H. Zhang, C. Guo, X. Su, C. Zhu, Measurement data fitting based on moving least squares method, Mathematical Problems in Engineering 2015 (2015) 1–10. doi:10.1155/2015/195023.

[35] L. Ramírez, C. Foulquié, X. Nogueira, S. Khelladi, J.-C. Chassaing, I. Colominas, New high-resolution-preserving sliding mesh techniques for higher-order finite volume schemes, Computers & Fluids 118 (2015) 114–130. `doi:10.1016/j.compfluid.2015.06.008`.

[36] K. Masatsuka, I do like CFD, VOL.1, Second Edition, no. v. 1, K. Masatsuka, 2013.

[37] P. Woodward, P. Colella, The numerical simulation of two-dimensional fluid flow with strong shocks, Journal of Computational Physics 54 (1) (1984) 115–173. `doi:10.1016/0021-9991(84)90142-6`.

[38] E. F. Toro, C. E. Castro, B. J. Lee, A novel numerical flux for the 3d euler equations with general equation of state, Journal of Computational Physics 303 (2015) 80–94. `doi:10.1016/j.jcp.2015.09.037`.

[39] C.-W. Shu, S. Osher, Efficient implementation of essentially non-oscillatory shock-capturing schemes, II, Journal of Computational Physics 83 (1) (1989) 32–78. `doi:10.1016/0021-9991(89)90222-2`.

[40] C. W. Schulz-Rinne, J. P. Collins, H. M. Glaz, Numerical solution of the riemann problem for two-dimensional gas dynamics, SIAM Journal on Scientific Computing 14 (6) (1993) 1394–1414. `doi:10.1137/0914082`.

[41] P. D. Lax, X.-D. Liu, Solution of two-dimensional riemann problems of gas dynamics by positive schemes, SIAM Journal on Scientific Computing 19 (2) (1998) 319–340. `doi:10.1137/s1064827595291819`.

[42] C.-Y. Jung, T. B. Nguyen, Fine structures for the solutions of the two-dimensional riemann problems by high-order WENO schemes, Advances in Computational Mathematics`doi:10.1007/s10444-017-9538-8`.

[43] H. W. Liepmann, A. Roshko, Elements of gasdynamics, AIChE Journal 5 (2) (1959) 8J–8J. `doi:10.1002/aic.690050234`.

[44] N. Botta, R. Jeltsch, A numerical method for unsteady flows, Applications of Mathematics 40 (3) (1995) 175–201. `doi:http://dx.doi.org/10.3929/ethz-a-004284212`.

[45] C. Kim, 5th international workshop on high-order cfd methods inviscid strong vortex shock wave interaction, `https://web.archive.org/web/20170830105138/https://how5.cenaero.be/sites/how5.cenaero.be/files/CI2_StrongVortexShock_0.pdf`.

[46] J. S. Park, H. You, C. Kim, Higher-order multi-dimensional limiting process for DG and FR/CPR methods on tetrahedral meshes, Computers & Fluids 154 (2017) 322–334. `doi:10.1016/j.compfluid.2017.03.006`.

[47] H. C. Yee, P. Kutler, Application of second-order-accurate total variation diminishing (tvd) schemes to the euler equations in general geometries, NASA Technical Memorandum 85845.

[48] P. Roe, Approximate riemann solvers, parameter vectors, and difference schemes, Journal of Computational Physics 43 (2) (1981) 357–372. `doi:10.1016/0021-9991(81)90128-5`.

[49] A. Rohde, Eigenvalues and eigenvectors of the euler equations in general geometries, in: 15th AIAA Computational Fluid Dynamics Conference, American Institute of Aeronautics and Astronautics, 2001. `doi:10.2514/6.2001-2609`.